BRNO UNIVERSITY OF TECHNOLOGY
VYSOKÉ UČENÍ TECHNICKÉ V BRNĚ

FACULTY OF MECHANICAL ENGINEERING
FAKULTA STROJNÍHO INŽENÝRSTVÍ

INSTITUTE OF PHYSICAL ENGINEERING
ÚSTAV FYZIKÁLNÍHO INŽENÝRSTVÍ

PLASMONIC BIOSENSORS BASED ON EXTRAORDINARY OPTICAL TRANSMISSION
PLAZMONICKÉ BIOSENZORY ZALOŽENÉ NA ZVÝŠENÉ OPTICKÉ TRANSMISI

MASTER'S THESIS
DIPLOMOVÁ PRÁCE

AUTHOR — **Bc. Martin Dršata**
AUTOR PRÁCE

SUPERVISOR — **prof. RNDr. Jiří Petráček, Dr.**
VEDOUCÍ PRÁCE

BRNO 2017

VYSOKÉ UČENÍ TECHNICKÉ V BRNĚ
FAKULTA STROJNÍHO INŽENÝRSTVÍ

Zadání diplomové práce

Ústav:	Ústav fyzikálního inženýrství
Student:	**Bc. Martin Dršata**
Studijní program:	Aplikované vědy v inženýrství
Studijní obor:	Fyzikální inženýrství a nanotechnologie
Vedoucí práce:	**prof. RNDr. Jiří Petráček, Dr.**
Akademický rok:	2016/17

Ředitel ústavu Vám v souladu se zákonem č.111/1998 o vysokých školách a se Studijním a zkušebním řádem VUT v Brně určuje následující téma diplomové práce:

Plazmonické biosenzory založené na zvýšené optické transmisi

Stručná charakteristika problematiky úkolu:

Plazmonické struktury skládající se z periodického uspořádání nanodírek v tenké kovové vrstvě mohou vykazovat velmi zajímavý jev, tzv. zvýšenou optickou transmisi (extraordinary optical transmission, EOT). Jev lze využít k měření změn indexu lomu a tím i ke konstrukci biosenzorů zaměřených na detekci biomolekul. Práce se bude zabývat rigorózními simulacemi takových biosenzorů a výzkumem vlivu geometrických parametrů na jejich detekční vlastnosti.

Cíle diplomové práce:

1. Rešeršní studie zaměřená na využití jevu EOT při konstrukci biosenzorů.
2. Výběr vhodného typu senzoru s EOT: definice materiálového systému a volba vhodného uspořádání nanodírek. Kvalitativní popis vlastností zvoleného uspořádání.
3. Rigorózní simulace vybraného typu biosenzoru, výzkum vlivu geometrických parametrů na jeho citlivost a další případné detekční parametry.

Seznam literatury:

Ebbesen T. W., Lezec H. J., Ghaemi H. F., Thio T., Wolff, P. A. Extraordinary optical transmission through subwavelength hole arrays. (1998) Nature 391: 667–669

Ghaemi, H. F., Thio, T., Grupp, D. E., Ebbesen, T. W., Lezec, H. J. Surface plasmons enhance optical transmission through subwavelength holes. (1998) Phys Rev B 58: 6779–6782

Degiron, A., Ebbesen, T. W. The role of localized surface plasmon modes in the enhanced transmission of periodic subwavelength apertures. (2005) J Opt A Pure Appl Opt 7:S90–S96

Genet, C., Ebbesen, T. W. Light in tiny holes. (2007) Nature 445:39–46

Brolo, G., Gordon, R., Leathem, B., Kavanagh, K. L. Surface plasmon sensor based on the enhanced light transmission through arrays of nanoholes in gold films. (2004) Langmuir 20: 4813–4815

Ekşioğlu, Y., Cetin, A. E., Petráček, J. Optical response of plasmonic nanohole arrays: comparison of square and hexagonal lattices. (2016) Plasmonics 11:851–856.

Gordon, R. et al. A New Generation of Sensors Based on Extraordinary Optical Transmission. (2008) Accounts of Chemical Research 41:1049–1057.

Termín odevzdání diplomové práce je stanoven časovým plánem akademického roku 2016/17

V Brně, dne

L. S.

prof. RNDr. Tomáš Šikola, CSc. ředitel ústavu	doc. Ing. Jaroslav Katolický, Ph.D. děkan fakulty

ABSTRAKT

Tato diplomová práce se zabývá rigorózními simulacemi plazmonických biosenzorů založených na jevu zvýšené optické transmise. První část je věnována popisu fyzikálních jevů a poznatků, které tvoří základ pro studium vlastností plazmonických senzorů, a popisu výpočetní metody konečných prvků v časové oblasti, která je využita v této práci. Vlastní výsledky jsou uvedeny v další části, která se zabývá výzkumem citlivosti, rozlišení a dalších charakteristik zvoleného typu plazmonického sensoru, tvořeného sítí kruhových nanoděr v tenké zlaté vrstvě na substrátě nitridu křemíku, v závislosti na řadě jeho geometrických parametrů. Tyto závislosti jsou sledovány ve třech různých případech, a to senzoru umístěného ve vakuu, ponořeného ve vodě a v případě kdy je na zlatém povrchu umístěna tenká dielektrická vrstva, která reprezentuje přítomnost biomolekul uchycených na povrchu senzoru.

KLÍČOVÁ SLOVA

metoda konečných diferencí v časové oblasti, zvýšená optická transmise, plazmonické senzory, síť nanoděr

ABSTRACT

This diploma thesis deals with rigorous simulations of plasmonic biosensors based on the phenomenon of extraordinary optical transmission. The first part is devoted to the description of the physical phenomena and knowledge, that forms the basis for studying the properties of plasmonic sensors, and the description of the finite-difference time-domain numerical method, that is used for all simulations carried out in this work. Simulation results are listed in the next part of this thesis. Here, the sensitivity, resolution and other characteristics of the chosen type of plasmonic sensor, consisting of an array of circular nanoholes in a thin gold film on the silicon nitride substrate, on a number of its geometrical parameters is investigated. These dependencies are monitored in three different cases, namely a sensor placed in a vacuum, immersed in water and where a thin dielectric layer is present on the gold surface, mimicking the presence of biomolecules immobilized the surface of the sensor.

KEYWORDS

finite-difference time-domain, extraordinary optical transmission, plasmonic sensor, nanohole array

DRŠATA, Martin *Plazmonické biosenzory založené na zvýšené optické transmisi*: diplomová práce. Brno: Vysoké učení technické v Brně, Fakulta strojního inženýrství, Ústav fyzikálního inženýrství, 2015. 58 s. Vedoucí práce prof. RNDr. Jiří Petráček, Dr.

PROHLÁŠENÍ

Prohlašuji, že svou diplomovou práci na téma „Plazmonické biosenzory založené na zvýšené optické transmisi“ jsem vypracoval samostatně pod vedením vedoucího diplomové práce a s použitím odborné literatury a dalších informačních zdrojů, které jsou všechny citovány v práci a uvedeny v seznamu literatury na konci práce.

Jako autor uvedené diplomové práce dále prohlašuji, že v souvislosti s vytvořením této diplomové práce jsem neporušil autorská práva třetích osob, zejména jsem nezasáhl nedovoleným způsobem do cizích autorských práv osobnostních a jsem si plně vědom následků porušení ustanovení § 11 a následujících autorského zákona č. 121/2000 Sb., včetně možných trestněprávních důsledků vyplývajících z ustanovení § 152 trestního zákona č. 140/1961 Sb.

Brno ....

(podpis autora)

Acknowledgment

I would like to thank to my mother Jana, father Jan and my brother Tomáš. Without their love, patience and neverending support this thesis could not be ever done. Furthermore, I would like to thank to my supervisor prof. RNDr. Jiří Petráček, Dr. for his suggestions and hints during the course of this work, as well as his professional guidance. Last but not least, i would also like to thank to all my friends and colleagues, especially David and Josef, without whose help it would be difficult for me to finnish this work.

OBSAH

INTRODUCTION

The need for cheap and fast methods of diagnosis or recognition of biological structures is currently a very discussed topic. Modern diagnostic methods are either costly, slow or require a large database of parameters of the examined species [1]. One way to circumvent these problems could be provided by plasmonic biosensors that are based on the phenomenon of extraordinary optical transmission.

According to Bethe's theory from 1944 [2], the amount of light, that is transmitted through a small circular aperture in a thin gold film, decreases with the fourth power of wavelength of the incident light. However, in 1998, Ebbesen observed [3] that for certain wavelength of the incident light, in the case of array of such nanoholes, the amount of light transmitted is significantly greater than that assumed by Bethe's theory. This extraordinary optical transmission (EOT) is the result of excitation of surface plasmon polaritons (SPP's) on the surface of gold, and the wavelength at which we observe this phenomenon is very sensitive to the optical properties of the medium surrounding the metal surface [4, 5]. The shift of this resonance peak can then help us to determine the environment in which the sensor is located and for example what biomolecules are immobilized at the metal surface or in which solution is the sensor immersed in.

Through the years, many promising applications of nanohole arrays have been devised for wide range of scientific fields. These applications include, for example, polarization control using rectangular or eliptical holes [6, 7], filtering techniques for solar absorbers and thermal emitters [8, 9], Surface-Eenhanced Fluorescence (SEF) [10] and Raman Scattering (SERS) [11] and even enhancement of quantum effects [12].

However, the possible use of such systems for biosensing application caught a lot of attention since it could provide very cheap and fast method of label-free on-chip diagnosis for use for example in third world and developing countries [13]. Moreover, such devices could also be very small and portable and allow paralel biosensing of many biological species at the same time (up to 10^5 simultaneous measurements on 1 cm^2 sensor [1]).

The submitted thesis is focused on numerical simulations of a sensor, that is based on EOT and consists of an array of circular nanoholes perforated in a thin gold film on an silicon nitride substrate.

This work is divided into two parts: theoretical study of the physical principles needed to understand the problematics of plasmonic sensing and part, that is summarizing the results of the simulations

First chapter provides brief introduction to the electromagnetism of metals. Starting with Maxwell's equations, the basic principles of electromagnetic wave pro-

pagation and differences between ideal and real metals are described. The second chapter is dedicated to derivation of conditions, under whitch the surface plasmon polaritons (SPP's) can be excited, and derivation of some of their basic physical properties. Localized surface plasmons (LSP's) are briefly described here, and thus the chapter gives a basic overview of plasmonics. Chapter three is devoted to description of the EOT phenomenon, geometry and material system of usually used type of sensors, their sensitivity and resolution. Fourth chapter then summarizes the basic information about the finite-diference time-domain (FDTD) method, used for simulations of interactions of light with matter, including the basic computational algorithm, stability requirements and boundary conditions.

The second part shows the results of FDTD simulations performed on the chosen type of plasmonic sensor. The main subjects of interest are the choice of suitable type of nanohole array and the dependence of sensitivity, resolution and other parameters of the sensor on its geometrical parameters such as nanohole size, thickness of individual layers or the shape of the nanohole array.

1 ELECTROMAGNETISM OF METALS

This chapter is devoted to description of the most important facts and phenomena, which underlie the theory of surface plasmon polaritons. Starting with description of Maxwell's equation of macroscopic electromagnetism, the electromagnetic response of idealized and real metals is described. Chapter closes with introduction of volume plasmons.

1.1 Maxwell's equations and electromagnetic wave propagation

The interaction of light with metal structures can be completely described using the macroscopic Maxwell's equation, defined as follows [14–16]:

$$\nabla \times \vec{E} = -\frac{\partial \vec{B}}{\partial t}, \tag{1.1}$$

$$\nabla \times \vec{H} = \frac{\partial \vec{D}}{\partial t} + \vec{j}_F, \tag{1.2}$$

$$\nabla \cdot \vec{E} = \rho, \tag{1.3}$$

$$\nabla \cdot \vec{H} = 0. \tag{1.4}$$

These equations link the areal current density $\vec{j}_H$ and bulk density of electric charge ρ with the four macroscopic fields $\vec{E}$ (the electrical field), $\vec{D}$(the dielectric displacement), $\vec{H}$(magnetic field) and $\vec{B}$(magnetic induction).

By combining equations (1.1)-(1.2), we can obtain wave equation

$$\nabla \times \nabla \times \vec{E} = -\mu_0 \frac{\partial^2 \vec{D}}{\partial t^2}, \tag{1.5}$$

in time domain, that is describing wave propagation in vacuum. Here ϵ_0 and μ_0 a vacuum permitivity and vacuum permeability, respectively.

The four macroscopic fields are also tied to each other by means of material equations

$$\vec{D} = \epsilon \vec{E} + \vec{P}, \tag{1.6}$$

$$\vec{H} = \frac{1}{\mu_0}\vec{B} - \vec{M}, \tag{1.7}$$

where $\vec{P}$ represents polarization and $\vec{M}$ is magnetization. By considering nonmagnetic material, we can neglect magnetization $\vec{M}$, and therefore limit the description only to polarization vector $\vec{P}$, which describes the electric dipole moment inside of material per unit volume, that is caused by response of microscopic dipoles to changes of the electric field [15].

Macroscopic Maxwell's equations are also complemented by three microscopic equations

$$\vec{j} = \sigma \vec{E}, \tag{1.8}$$

$$\vec{B} = \mu_0 \mu_r \vec{H}, \tag{1.9}$$

$$\vec{D} = \epsilon_0 \epsilon_r \vec{E}, \tag{1.10}$$

where σ(electric conductivity), μ_r(relative permeability) and ϵ_r(relative permitivity, also known as dielectric function) are characteristic for given media. Equations (1.8)-(1.10) are describing a situation, where coefficients σ, μ_r and ϵ_r are independent on electromagnetic field, position and direction in material, and therefore describing linear, homogenous and isotropic material [14].

The dielectric constant $\epsilon(\omega) = \epsilon' + i\epsilon''$ is a frequency dependent complex fucntion, that is also linked to complex index of refraction with [17, 18]

$$n = n + i\kappa = \sqrt{\epsilon}, \tag{1.11}$$

where imaginary part of refractive index κ is called an extinction coefficient. From equation (1.11), we can explicitly get

$$\epsilon' = n^2 - \kappa^2, \tag{1.12}$$

$$\epsilon'' = 2n\kappa, \tag{1.13}$$

$$n^2 = \frac{\epsilon'}{2} + \frac{1}{2}\sqrt{\epsilon'^2 + \epsilon''^2}. \tag{1.14}$$

The extinction coefficient κ, and therefore the dielectric function determines the absorption of electromagnetic waves propagating in given media and is also connected to the absorption constant of the Beer's law, that is describing decay of the intensity of the light in medium, via $\alpha(\omega) = 2\kappa(\omega)\omega/c$ [14, 15].

1.2 Dielectric function of free electron gas

The optical properties of metals can be, over a large range of frequencies, well described by a plasma model [14]. In this model a gas of electrons with density of n moves freely against a background of charged atom cores. These electrons are oscillating if some external electromagnetic field is applied, and their movement is decelerated with respect to a characteristic relaxation time τ and collision frequency $\gamma = 1/\tau$ [18, 19].

To determine the dielectric function $\epsilon(\omega)$ of such gas of free electrons, we need to start with equation of motion of an electron in the plasma sea in presence of external electric field $\vec{E}$

$$m\frac{d^2\vec{x}}{dt^2} + \gamma m\frac{d\vec{x}}{dt} = -e\vec{E}. \tag{1.15}$$

Assuming harmonic and time-dependent external field $\vec{E} = \vec{E}_0 e^{-i\omega t}$ and considering that macroscopic polarization can be described as $\vec{P} = -ne\vec{x}$, it can be shown [19, 20], that

$$\vec{P} = -\frac{ne^2}{m(\omega^2 + i\gamma\omega)}\vec{E}. \tag{1.16}$$

Combining equations (1.6), (1.10) and (1.16), we simply get the resulting equation for dielectric function $\epsilon(\omega)$ as a function of frequency ω

$$\epsilon(\omega) = 1 - \frac{\omega_p^2}{\omega^2 + i\gamma\omega}, \tag{1.17}$$

where

$$\omega_p^2 = \frac{ne^2}{\epsilon_0 m}, \tag{1.18}$$

is the plasma frequency of the free electron gas. The real and imaginary parts of $\epsilon(\omega)$ are given by

$$\epsilon'(\omega) = 1 - \frac{\omega_p^2\tau^2}{1 + \omega^2\tau^2}, \tag{1.19}$$

$$\epsilon''(\omega) = \frac{\omega_p^2\tau^2}{\omega(1 + \omega^2\tau^2)}. \tag{1.20}$$

If we now consider only large frequencies close to ω_p where $\omega\tau >> 1$, then we can neglect the effect of collisions and immediately get an equation for dielectric function of the undamped free electron plasma as [19]

$$\epsilon(\omega) = 1 - \frac{\omega_p^2}{\omega^2}. \tag{1.21}$$

In the region of large frequencies $\omega\tau << 1$, where $\omega < \omega_p$, metals are mainly absorbing with an absorption coefficient of

$$\alpha = \sqrt{\frac{2\omega_p^2 \tau\omega}{c^2}}, \tag{1.22}$$

and the electromagnetic fields are damped inside of the metal exponentially as $e^{-z/\delta}$, where $\delta = 2/\alpha$ is a skin depth [16].

The dielectric function of the free electron plasma can be also linked with the classical Drude model for the conductivity of metals, defined as $\sigma = nep/m$, via

$$\epsilon(\omega) = 1 + \frac{i\sigma(\omega)}{\epsilon_0 \omega}, \tag{1.23}$$

and therefore $\epsilon(\omega)$ is the dielectric function of the free electron plasma also known as Drude model of the optical response of metals [15].

1.3 The dispersion of the free electron gas and volume plasmons

We will now consider a region of frequencies $\omega > \omega_p$. We can distinguish between two cases, depenging on polarization direction of the electric field vector $\vec{E}$. For transverse waves, where $\vec{k} \cdot \vec{E} = 0$, the dispersion relation in Fourier domain can be written as [15, 17]

$$k^2 = \epsilon(\vec{k}, \omega)\frac{\omega^2}{c^2}. \tag{1.24}$$

Longitidunal oscillations can only occur for frequencies corresponding to zeros of $\epsilon(\omega)$ [15]. By inserting equation (1.24) in equation (1.21), we can simply write a dispersion relation of travelling waves

$$\omega^2 = \omega_p^2 + k^2 c^2, \tag{1.25}$$

which is generally illustrated in Fig. 1.1. From Fig. 1.1 we can see, that the propagation of electromagnetic waves inside the metal plasma is only allowed for frequencies $\omega > \omega_p$. Such waves are then propagating with a group velocity given by $v_g = d\omega/dk < c$.

If we consider longitidunal oscillations of the electron sea against the background of (positive) atom cores (schematically in Fig. 1.1), the displacement u of the electron gas creates and electric field $\vec{E} = ne\vec{u}/\epsilon_0$ [15, 20], that acts as a restoring force.

The equation of motion of a unit of the electron gas is then

$$nm\frac{d^2\vec{u}}{dt^2} = -\frac{n^2 e^2 \vec{u}}{\epsilon_0}, \tag{1.26}$$

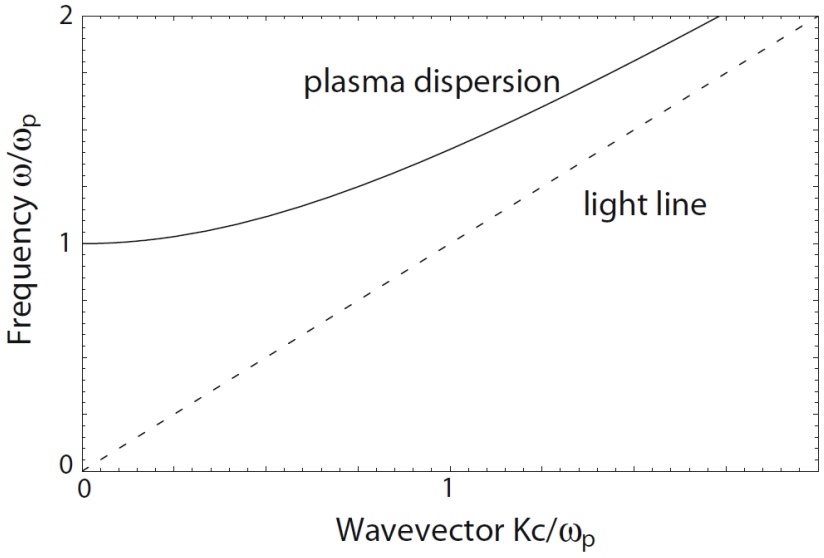

Fig. 1.1: Dispersion relation of free electron gas (solid black line) and light in vacuum (dashed black line). Taken from [16].

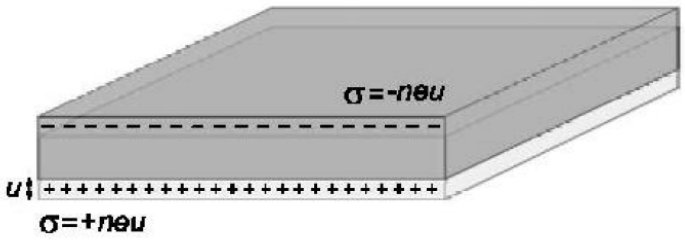

Fig. 1.2: Schematic interpretation of longitidunal collective oscillations of the condution electron gas in a metal slab. Taken from [15].

which is a equation of motion of a simple harmonic oscillator of the plasma frequency ω_p. Therefore, ω_p can be considered as the natural frequency of free oscillation of the electron gas. Here, we are assuming, that all electrons are moving in phase, and thus ω_p corresponds to oscillations where $\vec{k} = 0$ [14]. These oscillations can be only excited by particle impact and do not couple into transverse waves [15, 20]. Quantum of such oscillation is called a volume plasmon.

1.4 Real metals

Figure 1.3 shows the real and imaginary parts of dielectric function $\epsilon(\omega)$ for silver according to [21] and Drude model fit to the data. As can be seen, Drude model

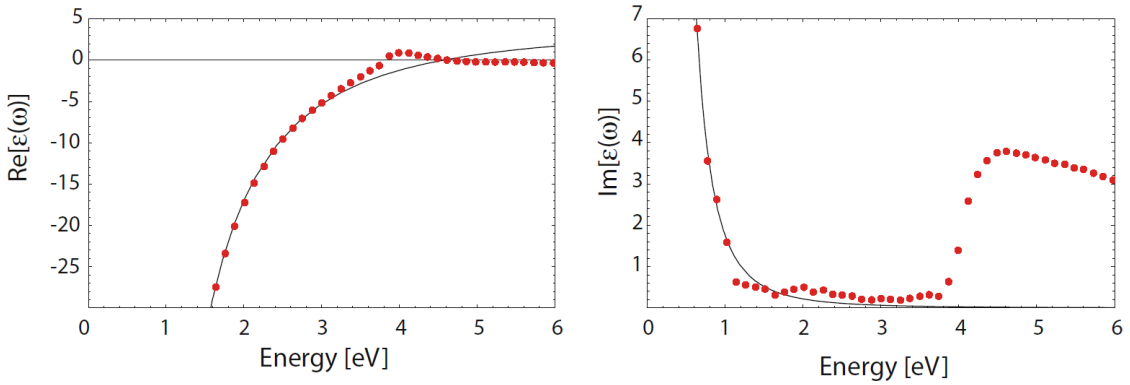

Fig. 1.3: Real and imaginary parts of dielectric function $\epsilon(\omega)$ for silver according to [21] (red dots) and Drude model fit (solid black line). Taken from [15].

is not precise for description of either ϵ_1 or ϵ_2 for higher frequencies (above the boundary between visible and near-infrared frequencies) in real metals like silver or gold, which are the most important materials in plasmonic studies.

Photons are very efficient in exciting electrons from band below the Fermi level to higher energy bands, and therefore inducing interband transitions, that are responsible for uncertainty of the Drude model in describing the dielectric function for real metals. These processes are also causing an increased damping of surface plasmons as well as a "competition" between the two excitations at visible frequencies.

While Drude model isn't really suitable for dexcription of $\epsilon(\omega)$, it's main advantage lies in the fact, that it can be very easily implemented into the time-domain based numerical methods. The problem of Drude model inadequacy can be overcomed if we dexcribe the interband transitions using the idea of a bound electron with resonance frequency ω_0. Equation (1.15) is then replaced by

$$m\frac{d^2\vec{x}}{dt^2} + \gamma m\frac{d\vec{x}}{dt} + m\omega_0^2\vec{x} = -e\vec{E}. \tag{1.27}$$

2 SURFACE PLASMON POLARITONS AND LOCALIZED SURFACE PLASMONS

In this chapter, the basic physical properties of propagating surface waves (surface plasmon polaritons, SPP's) and localized surface plasmons (LPP's) are described. The focus is primarily placed on the description and derivation of the basic properties of SPP's and methods of their optical excitation on planar metal-dielectric interfaces, since SPP's are playing the key role in this thesis.

2.1 SPP's on metal-dielectric interface

As indicated earlier, surface plasmon polaritons are electromagnetic wave excitations, that propagate along the surface of the metal-dielectric interface. To describe the basic physical properties of SPP's, we need to start, again, with Maxwell's equations (1.1)-(1.4).

We now assume harmonic time dependence of the electric field $\vec{E}(r,t) = \vec{E}_0(r)e^{-i\omega t}$, and that we can neglect the variation of dielectric function $\epsilon = \epsilon(r)$. By combining equations (1.1)-(1.2), as seen in Chapter 1, we can obtain the wave equation (1.5). Using the identities $\nabla \times \nabla \times \vec{E} = \nabla(\nabla \cdot \vec{E}) - \nabla^2\vec{E}$, and $\nabla \cdot (\epsilon\vec{E}) = \vec{E} \cdot \nabla\epsilon + \epsilon\nabla \cdot \vec{E}$, and considering that $\nabla \cdot \vec{D} = 0$, we can rewrite wave equation (1.5) into a Helmholtz equation defined as

$$\nabla^2\vec{E} + k_0^2\epsilon\vec{E} = 0, \tag{2.1}$$

where $k_0 = \omega/c$ is the wave vector of the propagating wave.

Next, we define geometry as shown in Fig. 2.1, where both the dielectric and metal layer are infinite in x-y plane at $z = 0$. We assume a one-dimensional problem, where surface waves propagate along the x-direction and show no variation along the y-direction. Therefore, the dielectric function can be defined as $\epsilon = \epsilon(z)$ and the propagating waves as $\vec{E}(x,y,z) = \vec{E}(z)e^{i\beta x}$, where $\beta = k_x$ is called a propagation constant. Equation (1.1) can be then rewritten as:

$$\frac{\partial^2\vec{E}_z}{\partial z^2} + (k_0^2\epsilon - \beta^2)\vec{E} = 0. \tag{2.2}$$

To derive the basic physical properties of SPP's and to define the conditions of their excitation, we need to solve (2.2) and Maxwell's curl equations (1.1)-(1.2) separately for the dielectric and metal halfspace. Such solutions are then connected through continuity conditions [14, 18], that are given by:

$$(\vec{D}_2 - \vec{D}_1) \cdot \vec{n} = 0, \tag{2.3}$$

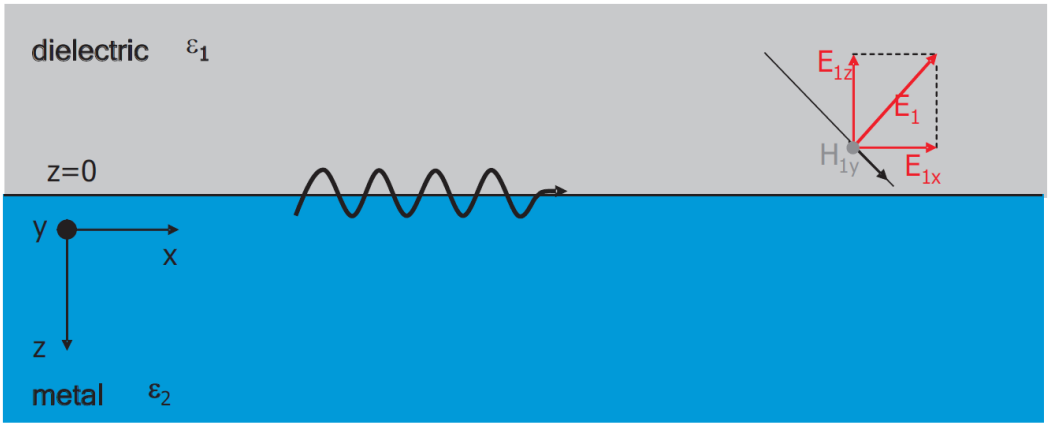

Fig. 2.1: Interface along the x-y plane between metal (index 2) and dielectric (index 1). Taken from [14].

$$(\vec{B}_2 - \vec{B}_1) \cdot \vec{n} = 0, \tag{2.4}$$

$$\vec{n} \times (\vec{E}_2 - \vec{E}_1) = 0, \tag{2.5}$$

$$\vec{n} \times (\vec{H}_2 - \vec{H}_1) = 0. \tag{2.6}$$

By combining the Maxwell's curl equations (1.1)-(1.2) and considering time harmonic ($\frac{\partial}{\partial t} = -i\omega$) wave propagating in x-direction ($\frac{\partial}{\partial x} = i\beta$), we can simply get [22] a set of coupled equations

$$\frac{\partial E_y}{\partial z} = -i\omega\mu_0 H_x, \tag{2.7}$$

$$\frac{\partial E_x}{\partial z} - i\beta E_z = i\omega\mu_0 H_y, \tag{2.8}$$

$$i\beta E_y = i\omega\mu_0 H_z, \tag{2.9}$$

$$\frac{\partial H_y}{\partial z} = i\omega\epsilon_0\epsilon E_x, \tag{2.10}$$

$$\frac{\partial H_x}{\partial z} - i\beta H_z = -i\omega\epsilon_0\epsilon E_y, \tag{2.11}$$

$$i\beta H_y = -i\omega\epsilon_0\epsilon E_z, \tag{2.12}$$

that will help us to find explicit expressions for each component of electric and magnetic field in both the metal and dielectric halfspace.

This system of equations allows two different solutions for different polarization of the propagating waves [15].

Transverse magnetic modes

First are the TM modes (transverse magnetic), where only the component of magnetic field, that is perpendicular to the direction of wave propagation is nonzero, and therefore $H_x = H_z = E_y = 0$. The set of equations (2.7)-(2.12) is, in this case, reduced to

$$E_x = -i\frac{1}{\omega\epsilon\epsilon_0}\frac{\partial H_y}{\partial z}, \tag{2.13}$$

$$E_z = -\frac{\beta}{\omega\epsilon\epsilon_0}H_y, \tag{2.14}$$

and the wave equation is

$$\frac{\partial^2 H_y}{\partial z^2} + (k_0^2\epsilon - \beta^2)H_y = 0. \tag{2.15}$$

Using the last set of equations (2.13)-(2.15) separately for both halfspaces gives

$$H_y(z) = A_2 e^{i\beta x}e^{-k_2 z}, \tag{2.16}$$

$$E_x(z) = iA_2\frac{1}{\omega\epsilon_2\epsilon_0}k_2 e^{i\beta x}e^{-k_2 z}, \tag{2.17}$$

$$E_z(z) = -A_2\frac{\beta}{\omega\epsilon_2\epsilon_0}e^{i\beta x}e^{-k_2 z}, \tag{2.18}$$

in dielectric halfspace ($z > 0$), and

$$H_y(z) = A_1 e^{i\beta x}e^{k_1 z}, \tag{2.19}$$

$$E_x(z) = -iA_1\frac{1}{\omega\epsilon_1\epsilon_0}k_1 e^{i\beta x}e^{k_1 z}, \tag{2.20}$$

$$E_z(z) = -A_1\frac{\beta}{\omega\epsilon_1\epsilon_0}e^{i\beta x}e^{k_1 z}, \tag{2.21}$$

in metal halfspace ($z < 0$). Continuity of the fields, as defined by equations (2.3)-(2.6), requieres that $A_1 = A_2$, and

$$\frac{k_2}{k_1} = -\frac{\epsilon_2}{\epsilon_1}. \tag{2.22}$$

Therefore if $\epsilon_2 > 0$, then $Re[\epsilon_1] < 0$.This means, that the surface waves can only exist on interfaces between materials that have opposite sign of the real parts of their relative permitivities, and therefore only on interfaces between the metals and insulators. If we consider, that H_y has to fulfill the wave equation (2.15), we can show [22, 23], that the dispersion relation for SPP's can be written as

$$\beta = \frac{\omega}{c}\sqrt{\frac{\epsilon_1\epsilon_2}{\epsilon_1 + \epsilon_2}}. \tag{2.23}$$

Transverse electric modes

It can be simply shown [14, 15], that similiar derivation, which we applied to the TM modes, leads in the case of TE (transverse electric, where $H_y = E_x = E_z = 0$) modes to condition

$$A_1(k_1 + k_2) = 0. \tag{2.24}$$

Because we require that $Re[k_1] > 0$ and $Re[k_2] > 0$, condition (2.24) is then only fulfilled when $A_1 = A_2 = 0$, and therefore $E_y = 0$. This means that, under these conditions, no TE surface modes can exist at metal-dielectric interface, thus surface plasmon polaritons only exist for TM polarization.

Reciprocal value of the wavevectors in z-direction $z = 1/|k_z|$ is called a skin depth [18] and represents,for given medium (defined by k_i), the evanescent decay length of the electromagnetic fields that are perpendicular to the plane of the interface, and therefore define the confinement of the surface wave.

2.2 Dispersion relation of SPP's and surface plasmons

If we consider that H_y, in case of TM modes, has to fulfill the wave equation (2.15), we can get [22, 23] expressions for wavevectors in both half spaces as

$$k_1^2 = \beta^2 - k_0^2\epsilon_1, \tag{2.25}$$

$$k_2^2 = \beta^2 - k_0^2\epsilon_2. \tag{2.26}$$

Combining (2.22), (2.25) and (2.26) leads immediately to the dispersion relation of the SPP's propagating along the metal-insulator interface

$$\beta = \frac{\omega}{c}\sqrt{\frac{\epsilon_1\epsilon_2}{\epsilon_1 + \epsilon_2}}. \tag{2.27}$$

Real and imaginary parts of this dispersion relation, for SPPs at the interface between a Drude metal with negligible collision frequency and air ($\epsilon_1 = 1$) and silica ($\epsilon_1 = 2,25$), is shown in Fig. 2.2 for frequencies ω normalized to the frequency ω_p.

In Fig. 2.2, SPP's correspond to the part of the dispersion curves, that lie to the right of the dispersion lines of air and silica, which means , that the SPP's cannot be excited on perfectly planar surface, and therefore some special excitation methods (discussed in Section 2.3) have to be applied [22]. As mentioned earlier, for frequencies $\omega > \omega_p$, metal becomes optically transparent allowing propagation of the electromagnetic waves inside the metal structure. In Fig. 2.2, we can also see a

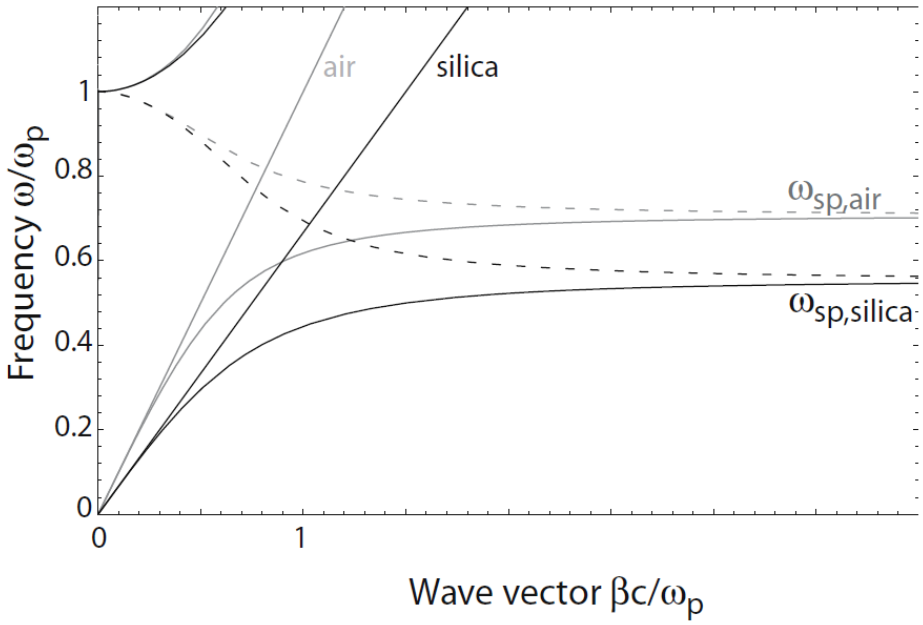

Fig. 2.2: Real (solid lines) and imaginary (dashed lines) parts of dispersion relation of SPPs at the interface between a Drude metal with negligible collision frequency and air (gray curves) and silica (black curves). Taken from [15].

frequency gap between the region of optical transparency and the region of propagating SPP's, where β is purely imaginary, allowing no propagation of electromagnetic waves at all.

The SPP frequency is, for large values of wavevectors, approaching a characteristic surface plasmon frequency. Equation for such frequencies can be obtained by inserting the expression for dielectric function of free electron (1.17) into the dispersion relation of the SPP (2.27), which yields

$$\omega_{sp} = \frac{\omega_p}{\sqrt{1+\epsilon_2}}. \tag{2.28}$$

If we consider neglectable damping of the oscillation of the free electron gas, then β goes to infinity for frequencies very close to ω_{sp} and group velicity goes to zero. Such mode gains electrostatic character and is called a surface plasmon.

2.3 Excitation of SPP's

As mentioned earlier, SPP's cannot be directly excited on planar surfaces by light beam propagating in a dielectric medium due to the fact, that the SPP wavenumber is larger than the magnitude of the wavevector of the light in dielectric medium.

This means that some special experimental arrangements has to be used in order to excite a wave propagating on metal-dielectric surface.

This section is dedicated to brief description of the most commonly used optical methods that provide the necessary wavevector conservation, thus allowing us to excite the SPP's.

Prism coupling

The most common and simple methods of SPP excitation are the prism coupling methods, that are matching the photon and SPP wavevectors using the tunneling photon in the total internal reflection of light (prism is illuminated at angle greater than the critical angle for total reflection) in prism.

Figure 2.3a shows the schematic illustration of the Kretchmann geometry, which is a method presented by Kretchsmann in 1971 [24]. Here, a thin metal film is illuminated through a prism at an angle greater than the angle of total internal reflection. In order to excite the SPP's, resonant condition

$$k_{sp} = \frac{\omega}{c}\sqrt{\epsilon_p}\sin\theta, \tag{2.29}$$

must be fullfilled. Here ϵ_p represents the permittivity of the prism and θ is the angle of incidence.

If condition (2.29) is fullfilled, a very sharp minimum of reflection at the metal-prism interface can be observed, and light can be coupled into SPP's with almost perfect efficiency. However, by using such method, SPP cannot be excited directly on the metal-prism interface [22]. This can be overcomed by creating additional dielectric layer (with refractive index smaller than the one of the prim) between the metal film and prism (schematically shown in Fig. 2.3b), which could provide resonant excitation of SPP on the inner interface, allowing us to excite both SPP modes at different angles of illumination.

For thick metal films, where Kretschmann configuration cannot be used (because the coupling of the tunneling photons is weaker with increasing thickness of the metal film), SPP's can be excited using the Otto configuration [25](schematically shown in Fig. 2.3c).

In Otto configuration, prism is placed very close to the surface. Photons are then tunneling through a thin air gap, allowing the excitation of SPP's directly on the metal-air interface. The resonant condition in Otto configuration is analogous to the one of Kretschmann configuration (2.29), [22, 26].

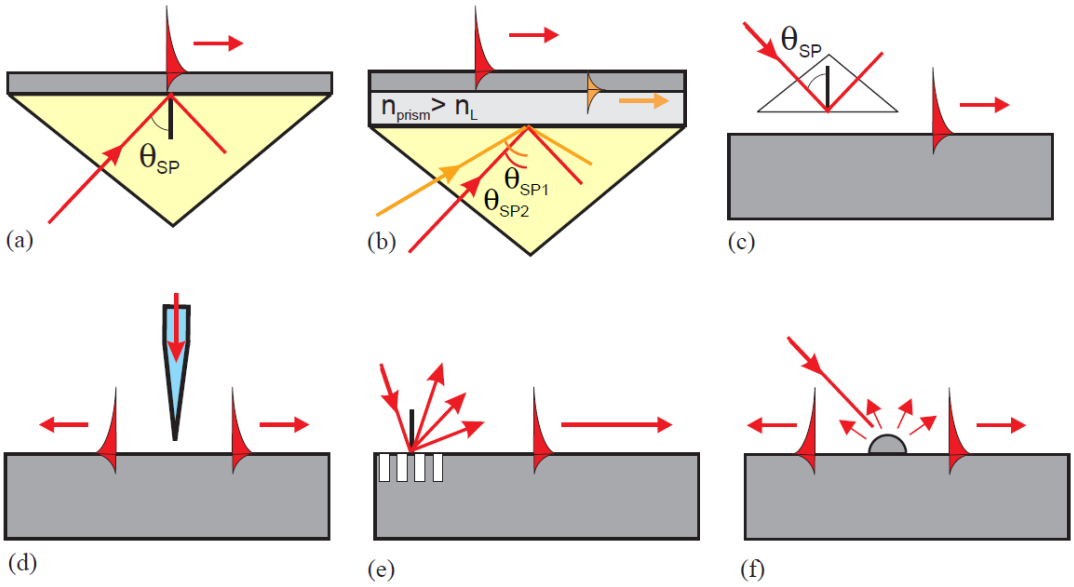

Fig. 2.3: Schematic representation of **a** Kretschmann configuration, **b** Two-layer Kretschmann geometry, **c** Otto configuration, **d** SNOM probe, **e** grating diffraction and **f** surface diffraction techniques for SPP excitation. Taken from [22]

Diffraction methods

Use of the diffraction effects on the randomly rough surface, some surface features or periodic diffraction grating can also provide the necessary wavevector conservation for SPP excitation.

Figure 2.3e shows schematic illustration of a diffraction grating created on a smooth metal surface. Light is diffracted upon incidence on such structure and the components of the diffracted light, whose wavevectors coincide with the SPP wavevector, are then coupled into SPP's. Such configuration can provide a very efficient method for excitation of SPP's on both, the air-metal and dielectric substrate-metal interfaces if the thickness of the metal layer and parameters of the grating are chosen appropriately [27, 28]. Condition for excitation of SPP's using diffraction grating is given by [22]

$$\vec{k}_{sp} = \frac{\omega}{c} n_s sin\theta \vec{u}_{12} \delta_p \pm p\frac{2\pi}{D}\vec{u}_1 \pm q\frac{2\pi}{D}\vec{u}_2, \tag{2.30}$$

where $\vec{u}_1$ and $\vec{u}_2$ are the unit lattice vectors of the periodic structure, D is its period, n_s is the refractive index of surrounding medium, $\vec{u}_{12}$ is the unit vector in direction of the in-plane component of the wavevector of incident light and δ_p equals one for p-polarized incident light and zero for s-polarized light.

In the case of randomly rough surface, the conditions for SPP excitation can be easily achieved without the need to use any experimental arrangement, because of

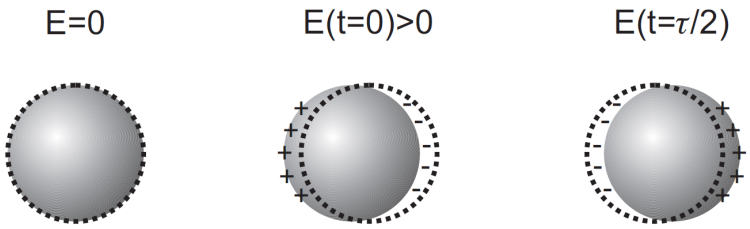

Fig. 2.4: LSP's on a metal nanoparticle in the absence (left) and presence (right) of the external electromagnetic field. Taken from [14]

the presence of the diffracted light components with all wavevectors [22]. However, since the SPP conditions are not well-defined, coupling of light into SPP efficiency is very low in this case and leads into a complex field distribution over the surface [22].

This problem can be overcomed by creating some well-defined surface features (such as shown in Fig. 2.3f) on smooth planar surface, that are giving the necessary "control"over the diffraction interactions of the incident light with surface, leading to better-defined excitation conditions, and therefore more efficient light-to-SPP coupling [22].

Near-field excitation

Another optical method of SPP excitation is the use of Scanning Near-field Optical Microscopy (SNOM), which is shown in Fig. 2.3d. Illumination through SNOM fiber tip can excite circular SPP waves locally at a chosen place on the surface [29]. This configuration can be considered both a tunneling and diffraction mechanism.

In the first case mentioned, the technique is analogous to the Otto configuration. The excitation process is here described with photon tunneling from the tip of the SNOM probe to the surface of the metal, but on the contrary to Otto configuration, SPP's can be excited locally at a position of the SNOM probe [29].

In the second case, one can consider excitation of SPP's as a near-field coupling of the light that is diffracted on the fiber SNOM tip into SPP's [22].

2.4 Localized surface plasmons

Another type of fundamental plasmonic exctitaion, that needs to be mentioned, are the localized surface plasmons (LSP's). LSP's are non-propagating surface wave excitations on metallic nanostructures, spectrally in the visible or near infrared regime.

Many physical effects that are associated with the LSP's can be described with very simple model. Figure 2.4 shows the LSP's on a metallic nanoparticle with nad without the presence of the external electromagnetic field. The field can penetrate into the volume and cause the shift of the electrons. The coherentely shifted electrons, along with the external field, can be considered as an oscillator defined by the effective electron mass, geometry of the particle and its charge density [14].

The electric field inside and outside such metallic nanoparticle as a function of dipole moment $\vec{p}$ that is induced in the sphere by the external field, is defined as [14]

$$\vec{E}_{in} = \frac{3\epsilon_1}{\epsilon_1 + 2\epsilon_2}\vec{E}_0, \tag{2.31}$$

$$\vec{E}_{out} = \vec{E}_0 + \frac{1}{4\pi\epsilon_0\epsilon_2}\frac{3\vec{n}(\vec{n}\cdot\vec{p}) - \vec{p}}{r^3}, \tag{2.32}$$

where $\vec{n}$ is the unit vector in direction of the point of interest and ϵ_1, ϵ_2 are the permittivities of the nanoparticle and surrounding medium, respectively. With the LSP present, the ability of the nanoparticle to either scatter or absorb electromagnetic waves is enhanced. This ability can be described with scattering and absorption cross sections σ_{scat}, σ_{abs} as follows [14]

$$\sigma_{scat} = \frac{8\pi}{3}k^4a^6\left(\frac{\epsilon_1 - \epsilon_2}{\epsilon_1 + 2\epsilon_2}\right)^2, \tag{2.33}$$

$$\sigma_{abs} = 4\pi ka^3\mathrm{Im}\left(\frac{\epsilon_1 - \epsilon_2}{\epsilon_1 + 2\epsilon_2}\right). \tag{2.34}$$

Here a is the radius of the nanoparticle. As can be seen, the scattering scales with a^6, while absorption process scale with a^3. Consequently, for large particles scattering dominates, whereas for smaller particles, extinction is dominated by absorption.

3 OPTICAL BIOSENSORS BASED ON EXTRAORDINARY OPTICAL TRANSMISSION

This chapter is dedicated to introduction of the plasmonic optical sensors that are based on principle of extraordinary optical transmission (EOT). Such sensors usually consists of an array of nanoholes in thin metal layer, that allows excitation of SPP's on the surface, and can be used in many applications.

Althought many promising applications of nanohole arrays have been devised for wide range of scientific fields [6, 8, 11], in this chapter, we will focus on the applications concerning hole-arrays in metal films as a tool for label-free sensing applications and diagnostics.

Chapter starts with a brief description of the EOT phenomena, which plays a key role in a plasmonic biosensing. Principle of the plasmonic sensing and conventional designs of such sensors is then introduced. Chapter closes with a definition of sensitivity and resolution of a nanohole array plasmonic sensors.

3.1 Extraordinary optical transmission

According to classical aperture theory by Bethe from 1944 [2], the amount of light, that is transmitted through circular hole in metal sheet, is proportional to

$$T \propto \frac{d}{\lambda^4}, \tag{3.1}$$

where λ is the wavelength of incident light and d is the hole diameter. However, in 1998 Ebbesen experimentaly observed [3] that, for certain wavelengths, the amount of light transmitted through periodical array of circular holes in gold thin film is significantly greater than predicted. This phenomenon can even be observed in cases, where the thickness of the metal film is greater than the skin depth. Example of such extraordinary optical transmission (EOT) is shown in Fig. 3.1.

The EOT occurs through certain interactions of surface plasmon polaritons, that are excited on the surface of the metal film, with the light incident on the surface at some specific wavelength. If we consider a plane wave incident on the metal surface, the resonant wavelength, corresponding to the EOT peak, can be directly derived from Eequation (2.30), where $\sin\theta$=1 and δ_p=1, and is approximately given by [13, 31]

$$\lambda_{res} \approx \frac{a_0}{\sqrt{i^2+j^2}} \sqrt{\frac{\epsilon_m + \epsilon_d}{\epsilon_m \epsilon_d}}, \tag{3.2}$$

where a_0 is the distance between the holes, i, j are the grating orders and ϵ_m, ϵ_d are the permitivities of the metal and surrounding dielectric, respectively.

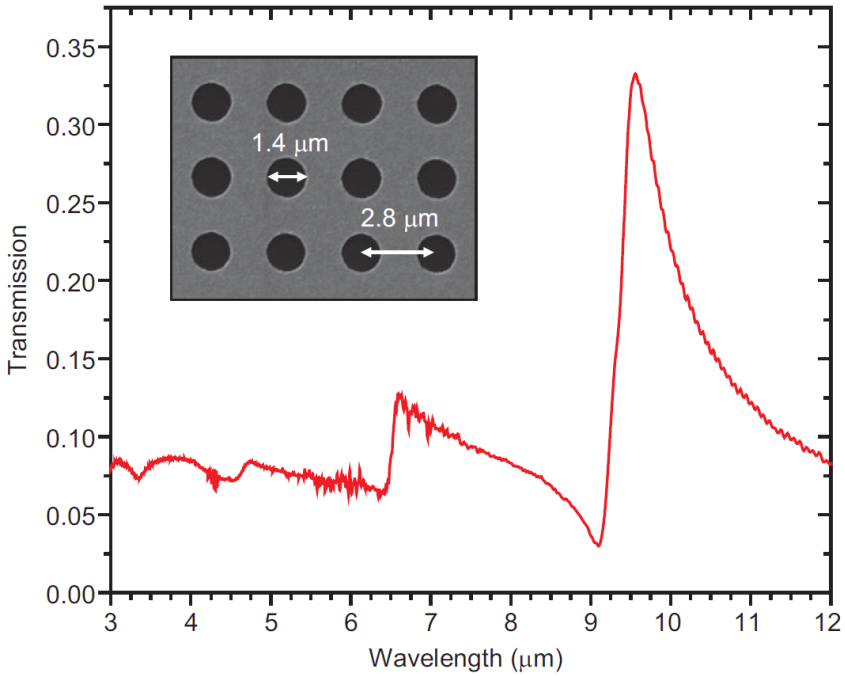

Fig. 3.1: Example of the transmission spectra through circular hole array in gold thin film on GaAs substrate. The EOT peak can be seen at wavelength of approximately 9.5 μm Taken from [30].

The equation (3.2) shows, that the position of the EOT peak is strongly dependent on the periodicity of the array, refractive index of the metal sheet and refractive index of the surrounding dielectric. The dependence of the EOT position on the ϵ_d is the characteristic, that plays the key role in plasmonic sensing application, as discussed in following Section.

3.2 Optical sensors based on EOT principle

Since the Ebbesen's work was first published [3], there has been wide research aimed at understanding and development of many applications asociated with the EOT phenomenon [32–34].

Motivation for plasmonic biosensing lies in the fact, that modern diagnostic methods are either expensive, slow, not portable devices or require a large parameter databases of the known biological species for diagnosis to be possible [13]. Plasmonic biosensors, on the other hand, could provide a methods of very fast yes-or-no label-free onchip diagnosis, that doesn't require any parameter database at all [33]. It could also give us the possibility of paralel biosensing of many biological species at the same time (up to 10^5 simultaneous measurements on 1 cm^2 sensor, according

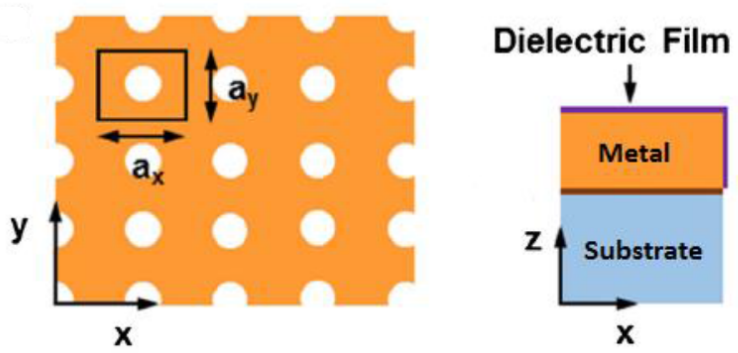

Fig. 3.2: Top view and cross section of an example of plasmonic sensor consisting of an lattice of circular holes with periodicities a_x, a_y in thin metal layer deposited on a dielectric substrate. Taken from [31]

.

to [1]). It is also considered a very cheap and portable device [33].

General example of a plasmonic sensor, which usually consists of nahohole array in a metal structure deposited on a dielectric substrate, is shown on Fig. 3.2. Through last two decades, many designs of a plasmonic biosensors were devised, including different shapes of holes [4, 35], types of arrays [36, 37] or types of metal-substrate structures [31, 38]. However, for biosensing applications, circular holes perforated through a gold thin film and either a square or hexagonal configuration of the hole array showed as the best performance and is today used almost exclusively [1,39–41].

Principle of such sensors is related to the fact, that the spectral position of the EOT peak λ_{res} is very sensitive to change of the refractive index of the medium surrounding the metallic structure, as was mentioned in previous section. Such change can be achieved by for example immobilizing some examined biological species on the surface of the sensor (as shown in Fig. 3.2) or immersing the whole system in some bulk medium. The resonance peak is then spectrally shifted and the size of this shift is proportional to the change of the optical properties of the surrounding medium, as shown in Fig. 3.3. By investigating this spectral shift, is then possible to determine what biological species is adsorbed on the surface (or in what medium is the sensor immersed in), because its size should be specific for every refractive index change.

Together with a number of designs, many different applications of plasmonic sensors have been developed in sensing and diagnostics. For example as a tool for protein-like structure recognition [42], detection of a viruses in red blood cells [43] or early cancer detection [33].

However, the inaccuracies in todays nanohole-array fabrication methods are the

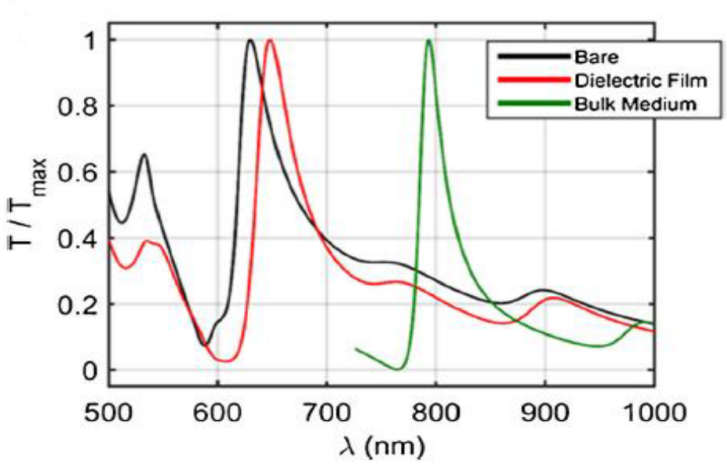

Fig. 3.3: An example of the transmission spectra of the bare plasmonic sensor in air (black line), bare sensor immersed in bulk medium (n=1.33, green line) and sensor after addition of 10 nm dielectric film (n=1.6, red line). Structure consists of square lattice (a_x=a_y=540 nm) of circular holes with a diameter of 200 nm in a 70 nm thick gold layer deposited on a 120 nm SiN substrate. Taken from [31]

reason of the main drawback of such systems. This is because of the disparity of the fabricated nanohole arrays, that reportedly causes a red shift of the resonance peak (in comparison to theoretically calculated values) [40], that can cause difficulties in quantitative evaluation of the results. However, the quality of the fabrication techniques is improving very quickly, and therefore the impact of these inaccuracies is steadily decreasing.

3.3 Sensitivity and resolution of nanohole arrays

The spectral sensitivity of a plasmonic sensors is given as [1]

$$S(\Delta\lambda_{res}) = \frac{\Delta\lambda_{res}}{\Delta n}, \tag{3.3}$$

where $\Delta\lambda_{res}$ is the shift of the EOT peak after addition of dielectric layer and Δn is the change of the effective refractive index of the surrounding medium. The spectral shift of the EOT peak $\Delta\lambda_{res}$ is dependent on the geometrical parameters of the nanohole array (periodicity, size of the holes, etc.), while Δn can be approximately defined as

$$\Delta n = (n_1 - n_2)(1 - e^{-2d/l_d}), \tag{3.4}$$

where d is the thickness of the dielectric layer, l_d is the characteristic decay length of the evanescent field and n_1, n_2 are the refractive indices of the adsorbed dielectric layer and the surrounding medium, respectively [1]. However, equation (3.4)

gives only the approximate expression for Δn, and therefore is not used in rigorous simulations using modern computational methods.

Another usefull parameter, that can define the sensing capabilities of the apertures is the figure of merit (FOM). The FOM is defined as the ratio between sensitivity and the linewidth of the EOT peak (FWHM), FOM=S/FWHM, which is an asset to consider the spectral properties of such system in addition to its sensing capability.

Simply, one can say, that the sensitivity of such sensors is given by the size of the spectral shift $\Delta\lambda_{res}$, while the resolution is proportional to the shape of the resonance peak, primarily the width of the resonance line and the sharpness of the peak.

Despite a number of advantages, the nanohole arrays generally shows lower resolution in comparison to the conventional surface plasmon resonance (SPR) sensors [3]. Devices, that are using the EOT, on the other hand, are usually affected by a very low signal-to-noise ratio, due to the fact, that the transmitted intensity is usually about 5% [37].

4 FINITE-DIFFERENCE TIME-DOMAIN (FDTD) METHOD

4.1 Introduction to FDTD method

The Finite-Difference Time-Domain (hereinafter FDTD) is one of the mostly used and straightforward computational methods for solving Maxwell's equations in differential form, and therefore many problems in electromagnetics for example electromagnetic absorption in human tissues [44], analysis of microstrip circuits [45] or electromagnetic scattering by ice crystals in atmosphere [46].

FDTD was first presented by Yee in 1966 [47] and it was initially designed for analyzing the two-dimensional scattering of TM pulses from cylindrical conductors. Method didn't attract much of attention until its first introduction in computer simulations in mid-seventies [48] when computer technologies, and therefore computational power had become more accessible. Since then, the FDTD is becoming increasingly popular for both, its conceptual simplicity and variability. With further increasing computational power and decreasing computational cost, the FDTD method is applied at problems that are associated with much shorter wavelenghts, letting us investigate the interaction of electromagnetic waves of still higher frequencies with still smaller structures.

The FDTD is based on discretizing Maxwell's equations in space and time to solve the electromagnetic scattering problem, therefore we create a grid scheme in which every point represents a component of electric and magnetic field in cartesian coordinates at a certain time.

By choosing correct initial conditions, we can calculate components of vectors of electromagnetic field at initial time, letting us, with certain accuracy, describe the evolution of the system in the future.

This discretization, however, shows us the main drawback of FDTD, which is that we need to perform computations over spatial domain that is often much larger then the investigated structure. This results in time consuming computations, especially for larger structures or simulations in which we require high precision [49].

4.2 Mathematical apparate

To derive equations, that are important for solving components of electric and magnetic field in certain time, we need to start with differential form of Maxwell's curl equations (1.1) and (1.2) that relates the electric and magnetic fields. By using the

rotation operator, we come to six equations for electric and magnetic field components of vectors in cartesian coordinates.

$$\frac{\partial E_x}{\partial t} = \frac{1}{\epsilon}\left(\frac{\partial H_z}{\partial y} - \frac{\partial H_y}{\partial z} - \sigma E_x\right), \tag{4.1}$$

$$\frac{\partial E_y}{\partial t} = \frac{1}{\epsilon}\left(\frac{\partial H_x}{\partial z} - \frac{\partial H_z}{\partial x} - \sigma E_y\right), \tag{4.2}$$

$$\frac{\partial E_z}{\partial t} = \frac{1}{\epsilon}\left(\frac{\partial H_y}{\partial x} - \frac{\partial H_x}{\partial y} - \sigma E_z\right), \tag{4.3}$$

$$\frac{\partial H_x}{\partial t} = \frac{1}{\mu}\left(\frac{\partial E_z}{\partial y} - \frac{\partial E_y}{\partial z}\right), \tag{4.4}$$

$$\frac{\partial H_y}{\partial t} = \frac{1}{\mu}\left(\frac{\partial E_x}{\partial z} - \frac{\partial E_z}{\partial x}\right), \tag{4.5}$$

$$\frac{\partial H_z}{\partial t} = \frac{1}{\mu}\left(\frac{\partial E_y}{\partial x} - \frac{\partial E_x}{\partial y}\right), \tag{4.6}$$

where ϵ is permitivity of the media, μ is permeability of the media and σ is electric conductivity.

In next step, we need to discretize equations(4.1) - (4.6). Mostly used way to do this, is to replace every derivatives in those equations by either central

$$\frac{\partial f}{\partial x} \approx \frac{f(x + \Delta/2) - f(x - \Delta/2)}{\Delta}, \tag{4.7}$$

forward

$$\frac{\partial f}{\partial x} \approx \frac{f(x + \Delta) - f(x)}{\Delta}, \tag{4.8}$$

or backward

$$\frac{\partial f}{\partial x} \approx \frac{f(x) - f(x - \Delta)}{\Delta}, \tag{4.9}$$

differences, where f is the derived function and Δ is the size of difference step, defined by size of space point of uniform, rectangular lattice, denoted as

$$(i, j, k) = (i\Delta x, j\Delta y, k\Delta z), \tag{4.10}$$

or any chosen time step Δt.

Because they are simply programmed and second-order accurate in both space and time, the central difference is usually chosen for discretization [47, 50].

Applying the (4.7) onto the set of equations (4.1)-(4.6), we get six scalar equations

$$E^{n+1}_{x,i,j,k} = \left(\frac{1-\sigma\Delta t/2\epsilon}{1+\sigma\Delta t/2\epsilon}\right) E^{n}_{x,i,j,k} + \left(\frac{\Delta t/2\epsilon}{1+\sigma\Delta t/2\epsilon}\right) \times \\ \times \left(\frac{H^{n+1/2}_{z,i,j+1/2,k} - H^{n+1/2}_{z,i,j-1/2,k}}{\Delta y} - \frac{H^{n+1/2}_{y,i,j,k+1/2} - H^{n+1/2}_{y,i,j,k-1/2}}{\Delta z}\right), \tag{4.11}$$

$$E^{n+1}_{y,i,j,k} = \left(\frac{1-\sigma\Delta t/2\epsilon}{1+\sigma\Delta t/2\epsilon}\right) E^{n}_{y,i,j,k} + \left(\frac{\Delta t/2\epsilon}{1+\sigma\Delta t/2\epsilon}\right) \times \\ \times \left(\frac{H^{n+1/2}_{x,i,j,k+1/2} - H^{n+1/2}_{x,i,j,k-1/2}}{\Delta z} - \frac{H^{n+1/2}_{z,i+1/2,j,k} - H^{n+1/2}_{z,i-1/2,j,k}}{\Delta x}\right), \tag{4.12}$$

$$E^{n+1}_{z,i,j,k} = \left(\frac{1-\sigma\Delta t/2\epsilon}{1+\sigma\Delta t/2\epsilon}\right) E^{n}_{z,i,j,k} + \left(\frac{\Delta t/2\epsilon}{1+\sigma\Delta t/2\epsilon}\right) \times \\ \times \left(\frac{H^{n+1/2}_{y,i+1/2,j,k} - H^{n+1/2}_{yx,i-1/2,j,k}}{\Delta x} - \frac{H^{n+1/2}_{x,i,j-1/2,k} - H^{n+1/2}_{x,i,j-1/2,k}}{\Delta y}\right), \tag{4.13}$$

$$H^{n+1/2}_{x,i,j,k} = \left(\frac{1-\Delta t/2\mu\sigma}{1+\Delta t/2\mu\sigma}\right) H^{n-1/2}_{x,i,j,k} + \left(\frac{\Delta t/\mu}{1+\Delta t/2\mu\sigma}\right) \times \\ \times \left(\frac{E^{n}_{y,i,j,k+1/2} - E^{n}_{y,i,j,k-1/2}}{\Delta z} - \frac{E^{n}_{z,i,j+1/2,k} - E^{n}_{z,i,j-1/2,k}}{\Delta y}\right), \tag{4.14}$$

$$H^{n+1/2}_{y,i,j,k} = \left(\frac{1-\Delta t/2\mu\sigma}{1+\Delta t/2\mu\sigma}\right) H^{n-1/2}_{y,i,j,k} + \left(\frac{\Delta t/\mu}{1+\Delta t/2\mu\sigma}\right) \times \\ \times \left(\frac{E^{n}_{z,i+1/2,j,k} - E^{n}_{z,i-1/2,j,k}}{\Delta x} - \frac{E^{n}_{x,i,j,k+1/2} - E^{n}_{x,i,j,k+1/2}}{\Delta z}\right), \tag{4.15}$$

$$H^{n+1/2}_{z,i,j,k} = \left(\frac{1-\Delta t/2\mu\sigma}{1+\Delta t/2\mu\sigma}\right) H^{n-1/2}_{z,i,j,k} + \left(\frac{\Delta t/\mu}{1+\Delta t/2\mu\sigma}\right) \times \\ \times \left(\frac{E^{n}_{x,i,j+1/2,k} - E^{n}_{x,i,j+1/2,k}}{\Delta y} - \frac{E^{n}_{y,i+1/2,j,k} - E^{n}_{y,i-1/2,j,k}}{\Delta x}\right), \tag{4.16}$$

that will allow us to determine the components of electric and magnetic field. With this system of equations the new value of field vector components at any space (lattice) point depends on its value and values of the components of different field vectors in previous time step. Therefore, at any given time step, as many parallel computations can proceed, as many processors are employed.

From the derivation of equations (4.11)-(4.16), we also see, that these equations can be easily expressed in different curvilinear coordinate systems, such as spherical or cylindrical coordinates. This can be usefull in problems where there is longitudinal or azimuthal symmmetry. Discretization process that leads to FDTD equations in polar, cylindrical and spherical coordinates is shown in [51].

4.3 Grid size and stability requirement

The FDTD algorithm solves the set of equations (4.11)-(4.16) in every point of chosen grid scheme repeatedly over time. Elementary cell (shown in Fig. 4.1) of such grid is called Yee cell [47].

For it's easy implementation, rectangular grids are usually chosen for most of the simulations. Also, they are not limited to certain geometries, but a curved surfaces are represented by "staircase"of rectangular cells, which can lead to various computational artifacts. To avoid such problems, many non-rectangular grids were devised [52–54].

Critical, for numerical accuracy and stability of the FDTD algorithm, are the sizes of spatial and time discretization steps, respectively. The size of spatial discretization steps must be such, that electromagnetic field doesn't significally change over one Yee cell. That means that the spatial discretization has to be as small as possible in comparison to the wavelength of the source to obtain higher accuracy. To achieve good numerical stability, we also need to consider suitable relation between the spatial and time increments. Such relation can be derived as follows.

Let us consider a discretized harmonic plane wave of real-valued frequency ω

$$f_{i,j,k}^{n} = f_0 e^{i(\omega n\Delta t - \beta_x i\Delta x - \beta_y i\Delta y - \beta_z i\Delta z)}, \tag{4.17}$$

where n is a discretization order and $\beta_{x,y,z}$ are the propagation constants. Such plane wave satisfies the wave equation

$$\frac{\delta^2 f}{\delta x^2} + \frac{\delta^2 f}{\delta y^2} + \frac{\delta^2 f}{\delta z^2} - \frac{1}{c^2}\frac{\delta^2 f}{\delta t^2} = 0. \tag{4.18}$$

By discretization of equation (4.18) using the central difference (4.7) and substitution of the plane wave (4.7) into the discretized wave equation, we get (after several modifications, tah can be found in [55])

$$\left[\frac{1}{c\Delta t}\sin\left(\frac{\omega\Delta t}{2}\right)\right]^2 = \left[\frac{1}{\Delta x}\sin\left(\frac{\beta_x\Delta x}{2}\right)\right]^2 + \left[\frac{1}{c\Delta y}\sin\left(\frac{\beta_y\Delta y}{2}\right)\right]^2 + \left[\frac{1}{c\Delta z}\sin\left(\frac{\beta_z\Delta z}{2}\right)\right]^2. \tag{4.19}$$

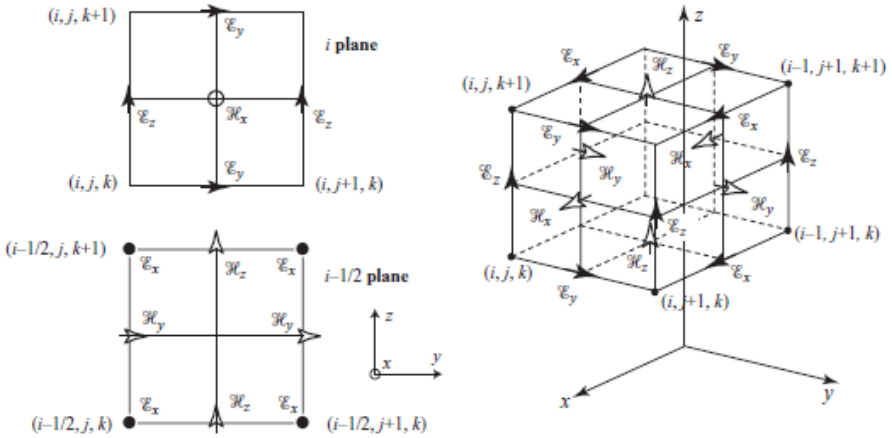

Fig. 4.1: Yee cell. At left are the slices of the cube at i and $i-1/2$, showing the field placement. Taken from [51].

We need the ω to be real, so the magnitude of the wave doesn't change its value exponentialy. This condition leads to

$$c\Delta t\sqrt{\frac{1}{\Delta x^2}\sin^2\left(\frac{\beta_x\Delta x}{2}\right)+\frac{1}{\Delta y^2}\sin^2\left(\frac{\beta_y\Delta y}{2}\right)+\frac{1}{\Delta z^2}\sin^2\left(\frac{\beta_z\Delta z}{2}\right)}\leq 1. \quad (4.20)$$

Considering the worst-case scenario (all sine functions equals one), we get the Courant-Friedrich-Levy (CFL) condition

$$\Delta t \leq \frac{1}{c\sqrt{\frac{1}{\Delta x^2}+\frac{1}{\Delta y^2}+\frac{1}{\Delta z^2}}} \quad (4.21)$$

where v_{max} is the maximum wave velocity in given media. The CFL condition describes the relationship between space and time increments of the simulation grid, that should be adjusted, for the stability of the simulations. For 3-D problems, the accuracy criteria approximately yields [55]

$$\Delta h \leq \frac{\lambda_{min}}{9\sqrt{3}} \approx \frac{\lambda_{min}}{16}, \quad (4.22)$$

where λ_{min} is the minimum wavelength in given media.

4.4 Boundary conditions

Because of the discretization character of FDTD, we need to work in a limited volume surrounding the investigated structures, thus we need to choose appropriate boundary conditions, that will define the edge of the volume.

The mostly used types of boundary conditions for various electromagnetic scattering problems are described in this section. The main focus is on description of symmetric and antisymmetric boundary conditions and the Uni-axial Perfectly Matched Layers, since those methods were used for simulations carried out in this thesis.

4.4.1 Uni-axial Perfectly Matched Layers (UPML) absorbing boundary conditions

For many wave-structure interaction problems it is important to define boundary conditions that absorb any outgoing waves, allowing as small reflection of waves back into the simulation area as possible. Since the initial work of K.S.Yee [47], many various techniques have been developed for absorption of outgoing waves.

The first method was the Radiating Boundary [56] but it was soon left unused due to its need for large simulation domains. Another two methods, both developed in late 1970's, were the one-way approximation of the wave equation, known as the Mur Boundary [44, 45, 48, 51, 57] and Matched Layer [51, 58], which consisted of a special absorbing medium surrounding the computational domain. Although both of these methods were still facing the problem that the wave is absorbed without reflection only in specific cases (for example when the outgoing wave is a plane wave and propagates perpendicularly to the boundary), they were the most commonly used until Berenger presented Perfectly Matched Layers (PML) absorbing boundary conditions in 1994 [59].

The PML gained a lot of attention very soon and is still the most used type of absorbing boundary conditions until today. Since Berenger's work, many interpretations of PML for various applications were introduced, for example Strech-Coordinate PML (SC-PML) [60], Convolutional PML [51] and Un-Split PML [61].

Nowadays, the most frequently used type of PML are the Uni-axial Perfectly Matched Layers (UPML) [51,62,63]. This method is based on introduction of anisotropic absorbing medium consisting of perfectly matched layers at a chosen plane on the edge of the computational domain. To match a UPML layer to some isotropic half-space, that is defined by its conductivity σ and permitivity ϵ, the time-harmonic Maxwell's equations can be interpreted as [63]

$$\nabla \times \vec{E}(x,y,z) = -i\omega\mu_0 \hat{s} \vec{H}(x,y,z), \tag{4.23}$$

$$\nabla \times \vec{H}(x,y,z) = (i\omega\epsilon_0\epsilon + \sigma)\hat{s}\vec{E}(x,y,z). \tag{4.24}$$

The tensor $\hat{s}$ is defined as

$$\hat{s} = \begin{bmatrix} s_y s_z s_x^{-1} & 0 & 0 \\ 0 & s_x s_z s_y^{-1} & 0 \\ 0 & 0 & s_x s_y s_z^{-1} \end{bmatrix}, \tag{4.25}$$

where $s_i = \kappa_i + \frac{\sigma_i}{i\omega\epsilon_0}$ and κ_i, σ_i are permitivity and conductivity independent UPML parameters, that are defined in the UPML region as follows:

1. In layers at both edges of computational domain along one axis, components of σ that are perpendicular to this axis equals zero and the same components of κ equals one (for example in layers along the x-axis, we have $\sigma_y = \sigma_z = 0$ and $\kappa_y = \kappa_z = 1$).
2. At overlapping dihedral corners of the UPML, component of σ that is perpendicular to both axes equals zero and the same components of κ equals one.
3. At overlapping trihedral corners of the UPML, the complete tensor (4.25) is used.

Several profiles of non-zero values of σ and to them corresponding values of κ were devised for minimalization of the reflection from UPML, but a polynomial grading of those parameters is usually chosen [51, 61, 63]. For example

$$\sigma_x(x) = \left(\frac{x}{d}\right)^m \sigma_{x,max}, \tag{4.26}$$

$$\kappa_x(x) = 1 + \left(\frac{x}{d}\right)^m (\kappa_{x,max} - 1), \tag{4.27}$$

where x is the position in the UPML and d is the UPML layer thickness in x direction. Parameter m is a real number with optimal values, found through experiments, between 3 and 4 [51].

The UPML equations are modifiyng the set of equations (4.11) - (4.16) that are used to determine the components of electric and magnetic field in the nodal points of the FDTD grid. Derivation of such modified equations using equations (4.23) - (4.25) is not trivial at all and is described in [63]. Examples of the equations for the x components of electric and magnetic field in the UPML region are then

$$\begin{aligned} E_x^{n+1}(i+1/2,j,k) &= \left(\frac{2\epsilon_0\kappa_z - \sigma_z\Delta t}{2\epsilon_0\kappa_z + \sigma_z\Delta t}\right) E_x^n(i+1/2,j,k) + \\ &+ \left(\frac{1}{2\epsilon_0\kappa_z + \sigma_z\Delta t}\right) \times [(2\epsilon_0\kappa_x + \sigma_x\Delta t)Q_x^{n+1}(i+1/2,j,k) - \\ &-(2\epsilon_0\kappa_x - \sigma_x\Delta t)Q_x^n(i+1/2,j,k)], \end{aligned} \tag{4.28}$$

$$H_x^{n+1/2}(i,j+1/2,k+1/2) = \left(\frac{2\epsilon_0\kappa_z - \sigma_z\Delta t}{2\epsilon_0\kappa_z + \sigma_z\Delta t}\right) H_x^{n-1/2}(i,j+1/2,k+1/2) +$$
$$+ \left(\frac{1/\mu}{2\epsilon_0\kappa_z + \sigma_z\Delta t}\right) [(2\epsilon_0\kappa_x + \sigma_x\Delta t)B_x^{n+1/2}(i,j+1/2,k+1/2) -$$
$$-(2\epsilon_0\kappa_x - \sigma_x\Delta t)B_x^{n-1/2}(i,j+1/2,k+1/2)], \tag{4.29}$$

where

$$Q_x(x,y,z) = \left(\frac{1}{s_y}\right)\left(\frac{s_y s_z}{s_x}\right) E_x(x,y,z). \tag{4.30}$$

Set of equations analogical to (4.28) and (4.29) is then applied only to the boundary layers and equations (4.11) - (4.16) are used in non-UPML region, in order to reduce the computational requirements.

4.4.2 Symmetric/antisymmetric boundary conditions

Symmetric and antisymmetric boundary conditions are a special techniques used in simulations of problems, where the electromagnetic fields have a plane of symmetry through the middle of the simulation region. By taking advantage of this symmetry, the computational time and the size of the simulation region required can be reduced by factor of two, four or even eight if the appropriate combination of symmetric and antisymmetric boundaries is chosen [64]. Therefore, such boundaries are useful for example for simulations that are based on interaction of a plane wave with periodic structures.

If the electromagnetic fields have a plane of symmetry, certain components of the electric and magnetic fields have to be zero at this symmetry plane. Symmetric and antisymmetric boundary conditions are implemented by forcing the appropriate field components to zero as shown in Fig. 4.2a.

As can be seen in Fig. 4.2a, normal electric field component and tangential magnetic field components have non-zero values, while tangential components of electric field and normal component of magnetic field are zero at a symmetric boundary. For antisymmetric boundaries, it is quite the opposite. The components of magnetic and electric fields are governed by certain rules of symmetry [64], shown in Fig. 4.2b, because of the reflections through the planes of symmetry.

From Fig. 4.2b, it can be seen, that if we choose appropriate boundary conditions in the middle of the simulation region, the symmetry will allow us to compute the fields only in one half-plane of the simulation region, and therefore reduce the grid size and computational time by one half. Furthermore if we have a problem

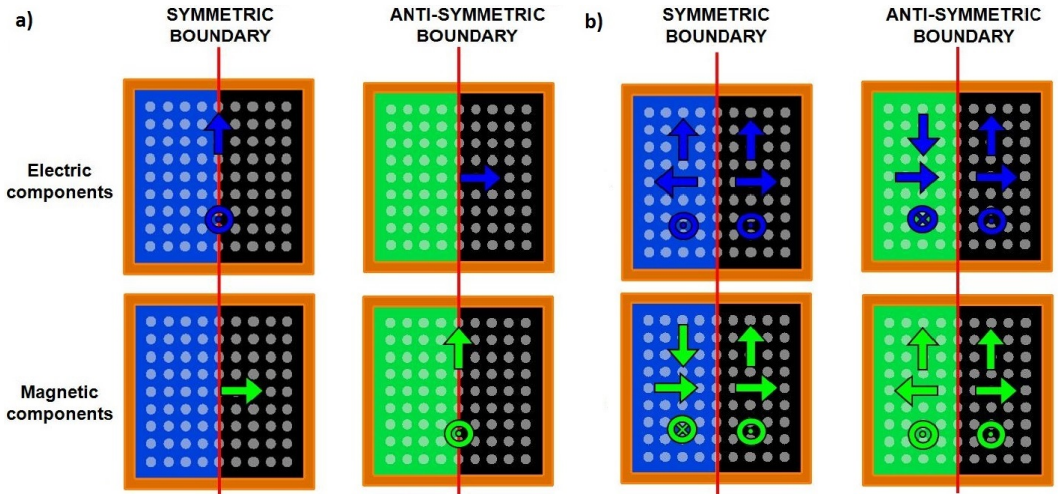

Fig. 4.2: **a** Non-zero electric (blue arrows) and magnetic (green arrows) field components at a symmetric and antisymmetric plane boundaries and **b** reflection symetry rules of electric (blue arrows) and magnetic (green arrows) field components at a symmetric and antisymmetric plane boundaries. Taken from [64].

with symmetry along two or three axes, we can reduce the computational time even more (by a factor of 4 in case of two-axes symmetry or by factor of 8 in case of three-axes symmetry) with appropriately chosen combinations of Symmetric and Antisymmetric Boundary Conditions, with respect to polarization of the input wave [64].

4.4.3 Other often used boundary conditions

Periodic boundary conditions

Periodic Boundary Conditions (PBC's) are the most often used boundary conditions for simulations of symmetric problems. PBC's are simply copying the electromagnetic fields that occur on one side of the simulation region and inject them back from the other side [64]. Therefore, we can calculate the response of the entire periodic system by simulating only one unit cell.

The popularity of this method lies in fact, that it is very straightforward and easy to implement [64–66], but its main drawback is, that a simulation with symmetry of both the EM fields and simulated structure itself is required. Therefore, the PBC's can be used for example when a symmetric periodic structure is illuminated by a plane wave propagating perpendiculary to the surface of the structure, but not if the source wave is propagating at an angle which would cause a phase shift on the sides of the computational domain [64].

Bloch boundary conditions

Bloch Boundary Conditions can be considered a more general form of PBC's. They aren't as easy to implement as PBC's but they apply a correction of the phase to the fields [64]

$$\vec{E}_{x,min} = e^{-ia_x\vec{k}_{bloch}}\vec{E}_{x,max}, \tag{4.31}$$

$$\vec{E}_{x,max} = e^{ia_x\vec{k}_{bloch}}\vec{E}_{x,min}, \tag{4.32}$$

where a_x is a distance between the boundaries of the computational domain along given axis and k_{bloch} is a Bloch wave vector, that is correcting the phase for diffferent angles of incidence overcoming the problem with sources propagating at an angle, that was mentioned in previous subsection.

Therefore, replacing PBC's with Bloch Boundary Conditions will not change the results of the simulations but give us a possibility to use more variable sources. Disadvantage of Bloch Boundary Conditions in comparison to PBC's is, that it requires approximately up to twice the computer memory and computational time [64].

5 SIMULATIONS AND RESULTS

This chapter is devoted to description of our sensor structure, simulation methods and to discussion of our simulation results. The goals of the simulations, presented in this thesis are

- Selection of a suitable type of EOT sensor: definition of the material system and choice of suitable nanohole array. A qualitative description of the properties of the selected layout,
- Rigorous simulations of the selected type of biosensor, investigation of the influence of the geometric parameters on its sensitivity and other possible detection characteristics, especially for the rectangular lattice of the nanohole array instead of the standard square configuration.

All FDTD calculations are performed in three dimensions using Lumerical FDTD solutions software [64]. The period of time, for wich is the FDTD algorithm caltulating the field development, is for all calculations chosen as $t = 2000$ fs and the step size is $\Delta t = 5$ fs.

5.1 Sensor structure and simulation parameters

Sensor structure

Figure 5.1 shows the schematic illustration of the sensor structure that was chosen for purposes of our simulations. All the selected parameters correspond to the real experiments [13,42,67] and can not be significantly changed for technological reasons.

Although silver has better optical properties for the use in plasmonic such sensors, 120 nm thick gold layer was chosen as a preferable material for our sensor, due to the reactive properties of silver. The nanohole array with periods a_x=a_y=540 nm along the x- and y-directions is made of circular holes with radius r=100 nm. The substrate is created by a 70 nm thick layer of silicon nitride. For constructional reasons, the Au and SiN layers are separated by a very thin 5 nm layer of Titanium. The dielectric functions of Au and Ti were taken from [68], the refractive index of SiN is set to $n_{SiN} = 2.16$.

Simulation parameters

The simulation setup, as exported from Luerical FDTD solutions, is shown on Fig. 5.2. The nanohole array is illuminated by a plane wave, propagating in z-

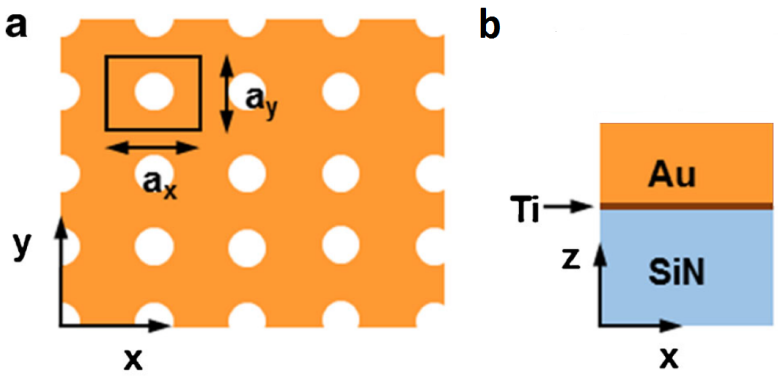

Fig. 5.1: **a** Top view and **b** cross section of the nanohole array. The array has periods a_x and a_y along the x- and y-directions. The device parameters, that were chosen as input values, are as follows: hole radius = 100 nm, array periodicity, $a_x = a_y = 540$ nm, and thicknesses of Au, Ti, and SiN layers of 120, 5, and 70 nm, respectively.

direction (as shown with wavevector $\vec{k}$) in the range of wavelengths from λ_{min}=500 nm to λ_{max}=1500 nm, with polarization in the x-direction (shown with the electric field $\vec{E}$). The material of the hole is chosen as ideal dielectric with refractive index corresponding to refractive index of the surrounding media (vacuum in basic setup).

Because the fields are symmetric along both, the x- and y-axes, the advantage of appropriately chosen combination of symmetric and anti-symmetric boundary conditions can be used. This allows us to simulate only one unit cell of the nanohole array, which will then describe the behaviour of theoretically infinite structure. The anti-symmetric boundary conditions were chosen for boundaries in y-z planes, symmetric boundary conditions in x-z planes and U-PML boundaries, to prevent reflection of the electromagnetic fields back into the simulation region, in x-y planes. This setup is reducing the computational time needed by a factor of four in comparison to periodic boundary conditions.

The simulation region is cubic with a sidelength of 540 nm, size of a FDTD Yee cell was chosen as 5 nm.

5.2 Bare nanohole array

In this section, we investigate the influence of some of the geometrical parameters of the nanohole array on the shape, heigth and full width at half maximum (FWHM) of the resonant peak, which are the characteristics that define the sensitivity and field of merit (FOM) of such structures.

We are discussing the characteristic changes in the resonance peak in comparison with geometrical setup as described in previous section, where the spectral position

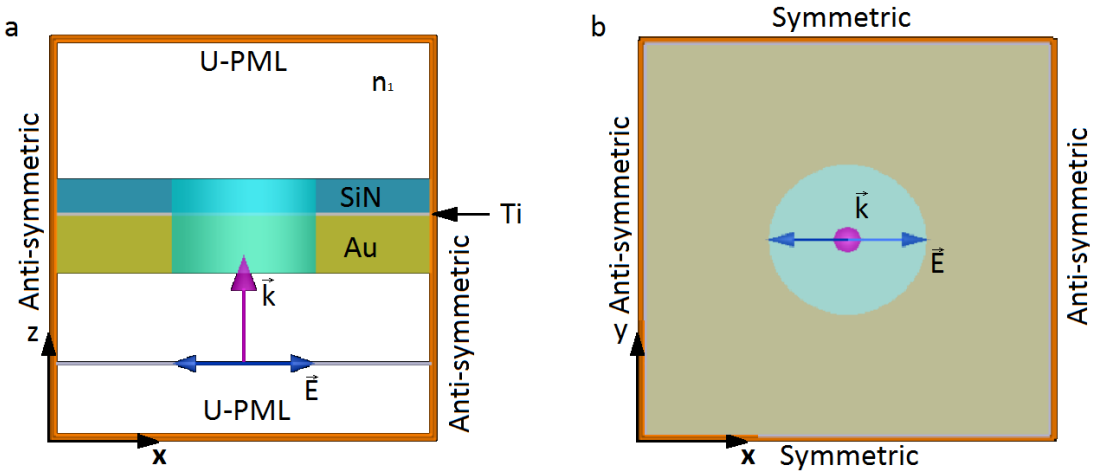

Fig. 5.2: **a** Cross section and **b** top view of the nanohole array exported from Lumerical FDTD solutions. Nanohole array is illuminated by a plane wave with polarization in the x-direction. anti-symmetric boundary conditions were chosen in the y-z planes, symmetric boundary conditions in the x-z planes and U-PML in x-y planes.

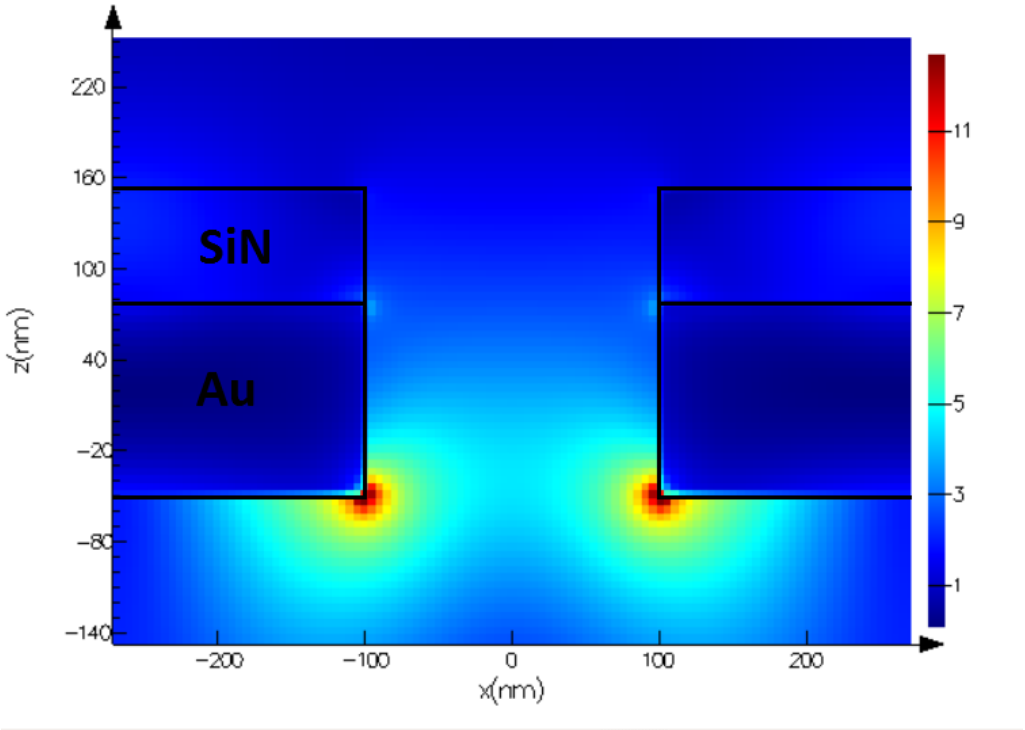

Fig. 5.3: Distribution of the electric field near the nanohole for λ_{res}=611.9 nm. Periodicities between the nanoholes are a_x=a_y=540 nm, diameter of the nanohole is 200 nm and the thicknesses of Au, Ti and SiN layers are 120, 5 and 70 nm respectively.

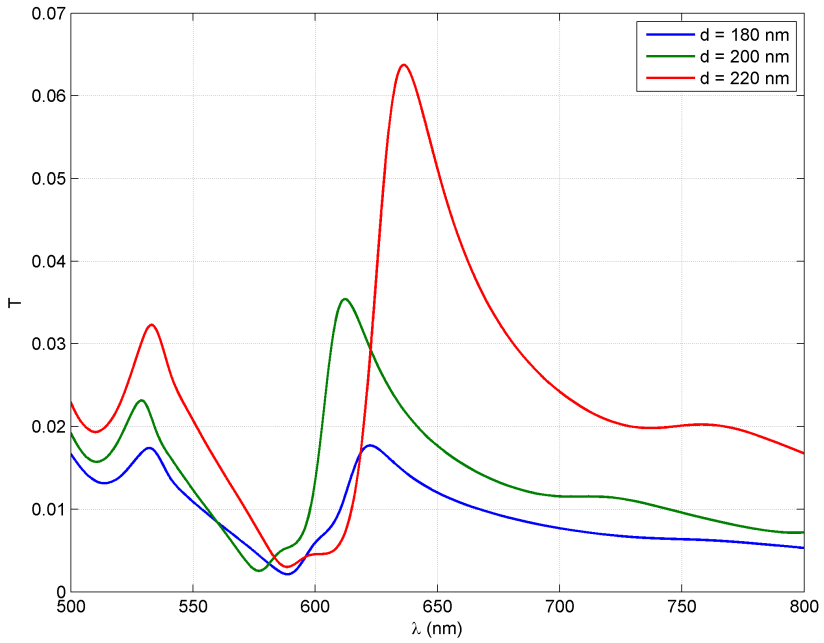

Fig. 5.4: Transmission spectra for nanohole arrays with hole diameters of 180 nm (blue), 200 nm (green) and 220 nm (red). Holes are penetrated through 120 nm of Au on a 70 nm SiN substrate, separated by 5 nm of Ti. Periodicities in both axes are $a_x = a_y$ =540 nm.

of EOT resonance is λ_{res}=611.9 nm, transmittance maximum of T_{max}=0.0354 and FWHM of 46.6 nm. The nanohole array is put in vacuum (n_1=1) and no dielectric layer on the Au surface is present.

Figure 5.3 shows the distibution of the electric field near the nanohole for λ_{res}=611.9 nm. The results show the surface plasmon resonance of the field, caused by interaction of the SPP's propagating on the gold surface, localized on the edge of the nanohole on the Au surface.

Hole diameter

Figure 5.4 shows the comparison of transmission spectra for diameters of holes of 180, 200, 220 nm. It can be seen, that for larger holes, the transmission peak is getting significantly stronger. Althought, the lowest value of FWHM (46.6 nm) corresponds to the hole diameter of d=200 nm (values of FWHM corresponding to hole diameters of d=180 nm and for d=220 nm are 60.8 nm and 54.3 nm, respectively), larger hole diameter can be still considered preferable choice since the change in the height of the transmission peak is much greater than the change of the FWHM value.

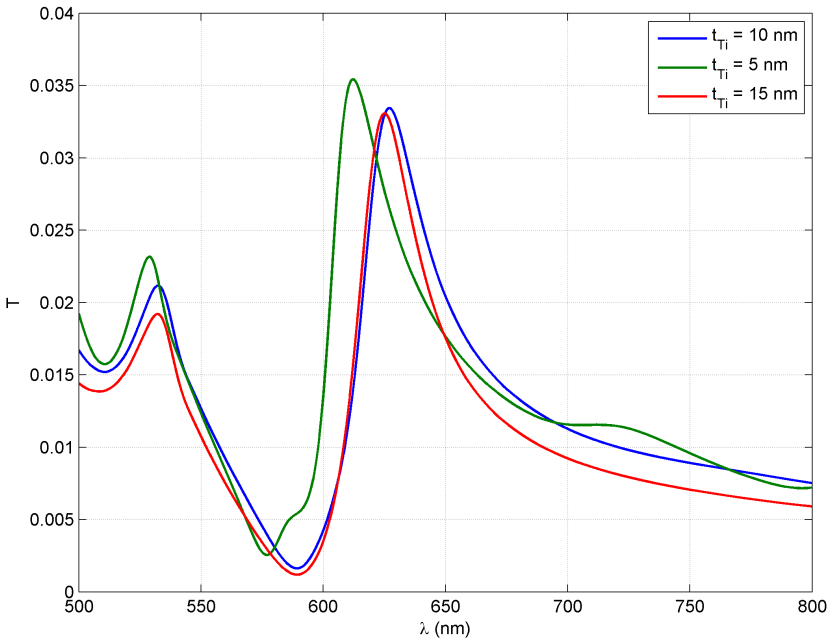

Fig. 5.5: Transmission spectra for nanohole arrays with thickness of Au layer of 120 nm on a SiN substrate with thickness of 70 nm separated by 5 nm (green), 10 nm (blue) and 15 nm (red) of Ti. Holes are of diameter 200 nm and periodicities in both axes are $a_x = a_y$ =540 nm.

However, the transmission peak size in comparison to non-resonant values is lower. Therefore, with further increasing the values of the hole diameters, the FWHM would be increasing much faster. This would, at some point, probably lead to total dissapearance of the EOT peak, so the size of the holes have to be chosen carefully.

Thickness of Au, SiN and Ti layers

The transmission spectra for several different values of Ti layer thickness are shown on Figure 5.5. Results show, that thiner layer of Ti should be preferable due to slightly higher transmission peak. However, the transmission spectra doesn't show any significant difference or FWHM values, which are 48.2, 46.6 and 41.1 nm for the thicknesses of 5, 10 and 15 nm, respectively.

In case of changing the Au layer thickness (Figure 5.6), the results show, that for thicker Au film, the resonance peak gets lower magnitude as well as much smaller FWHM (94, 46.6 and 41.5 nm for the thicknesses of 100, 120 and 140 nm, respectively). Because of this notable change of FWHM, thicker gold layer can be considered a better choice, since the decrease in transmission is not that significant and consi-

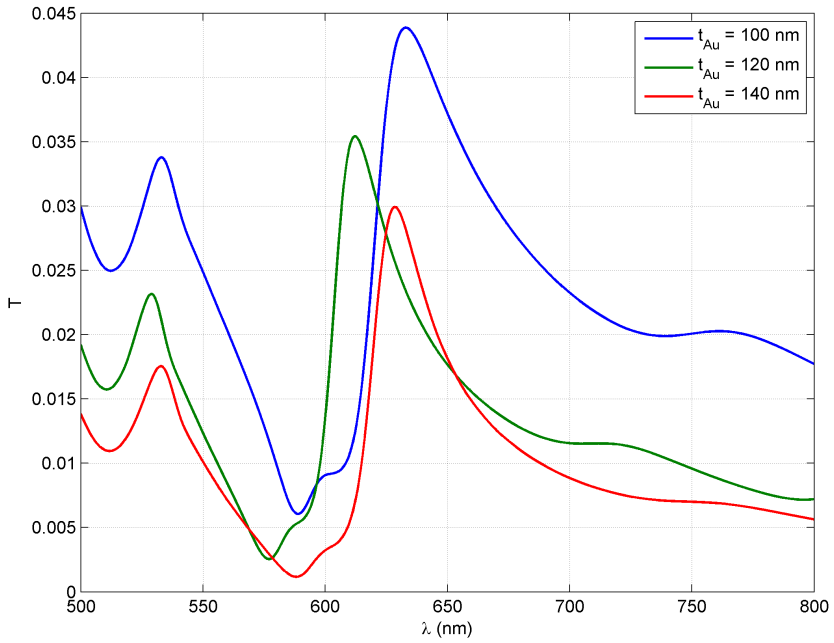

Fig. 5.6: Transmission spectra for nanohole arrays with thickness of the Au layer of 100 nm (blue), 120 nm (green) and 140 nm (red) on a 70 nm SiN substrate, separated by 5 nm of Ti. Holes are of diameter 200 nm and periodicities in both axes are $a_x = a_y$ =540 nm.

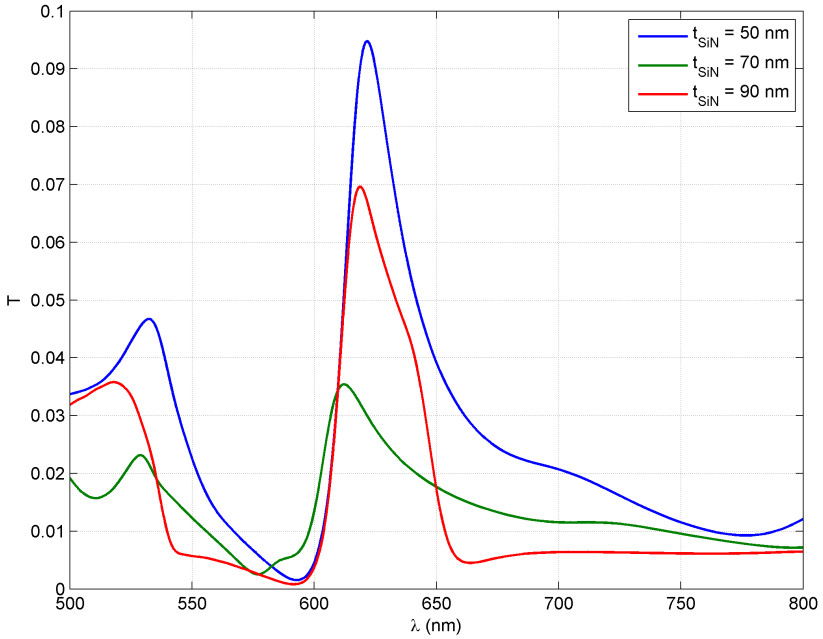

Fig. 5.7: Transmission spectra for nanohole arrays with thickness of Au layer of 120 nm on a SiN substrate with thicknesses of 50 nm (blue), 70 nm (green) and 90 nm (red) separated by 5 nm of Ti. Holes are of diameter 200 nm and periodicities in both axes are $a_x = a_y$ =540 nm.

dering, that transmission peak size in comparison to non-resonant values is greater.

Although larger thickness of Au film seems to be a better choice, it has to be, again, chosen carefully due to the fact, that for too thick metal film, no resonance in transmission could be observed at all.

Figure 5.7 shows the comparison of three transmission spectra for diferent thickness of the SiN. Here, thinner layer shows the best results due to the significant increase of the EOT peak heigth. The figure also shows enhancement of the FWHM(32.6, 46.6 and 33.7 nm for the thicknesses of 50, 70 and 90 nm, respectively) for both, increased and decreased thickness of the SiN layer in comparison to the original value of 70 nm. However, too thin SiN layer could cause a problems with fabrication of such sensor device.

Periodicity in x- and y-direction

Here, we investigate the effect of change of the periodicities a_x and a_y of the nanohole array along x- and y-axes. We are investigating the characteristics of the nanohole array with rectangular lattice, that define the sesitivity and FOM of such systems, in comparison to the standartly used square configuration. To simplify data interpretation, we denote parameter

$$\delta = a_y - a_x, \tag{5.1}$$

that defines the change of the nanohole array lattice against the square lattice configuration.

Examples of the transmission spectra for a_x=540 nm and different values of δ are shown on Fig. 5.8. We can see, that "well-defined" peaks are obtained for either large negative or large positive values of δ. This could mean that, by simple deviation from the square configuration of the nanohole array, we could allready significantly improve the sensing capabilities of the system.

However, a noticable phenomenon occurs in results, as one can see that, for a certain value of the δ parameter (around δ=20 nm), the resonance peak disappears and is replaced with another resonance, which is spectrally shifted to lower wavelengths. As we will show, this "splitting peak" phenomenon can be used at our advantage in order to further improve the sensitivity of the sensor and is widely discussed later in this chapter.

Figure 5.9a shows the transmission spectra of the nanohole array with square lattice configuration as a function of a_x and λ. The white dashed line represents the approximate values of the resonance wavelengths calculated by equation (3.2). It can be seen, that higher transmission peaks corresponds to lower values of a_x while

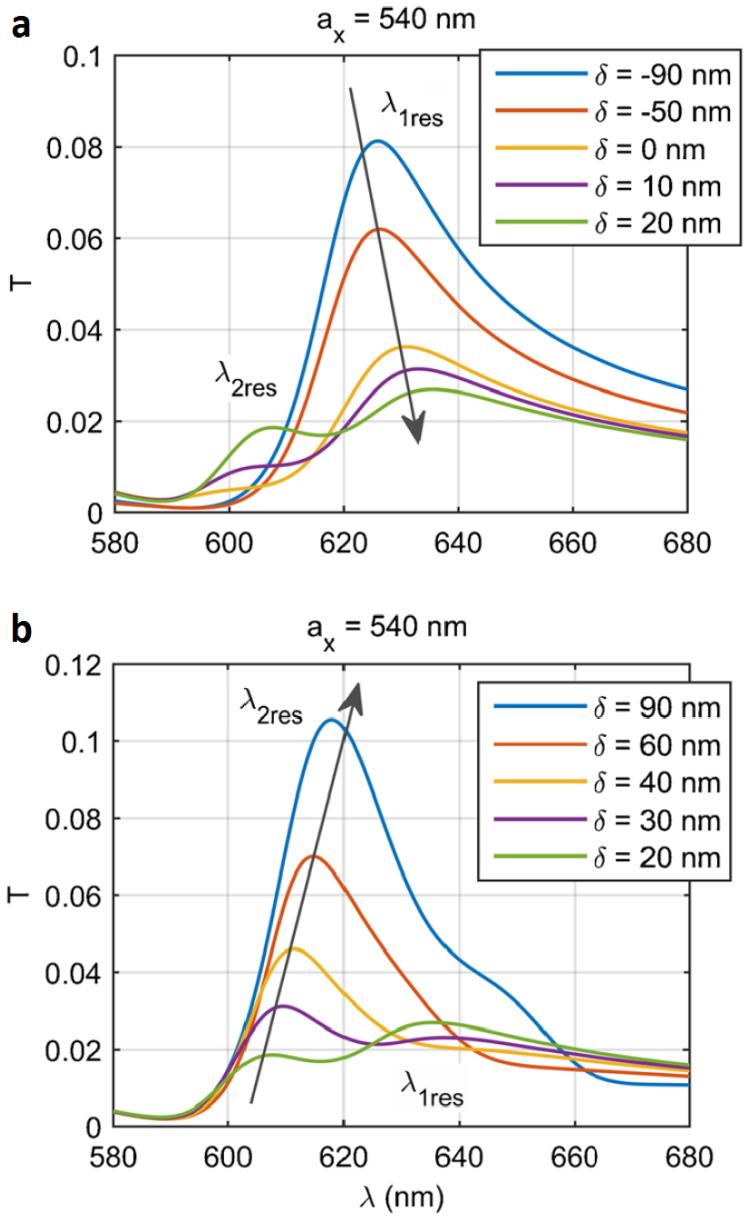

Fig. 5.8: **a**, **b** Transmission spectra of the bare nanohole array with periodicity along x-direction a_x=540 nm for different values of δ. Black arrows are showing the trend in the EOT resonance peak with increasing δ.

for higher values of a_x, the resonant peaks gets narrower. This forces us to choose the values that will be a compromise between the resonance power and its shape.

In comparison of those results with resulsts for different values of δ (shown on Fig. 5.9b and Fig. 5.10a), one can see, that the deviation from the square lattice leads, again, to the enhancement of the transmission efficiency and the resonance linewidth, especially for larger values of δ, where the resonance peaks are very significant and narrow (Fig. 5.10a).

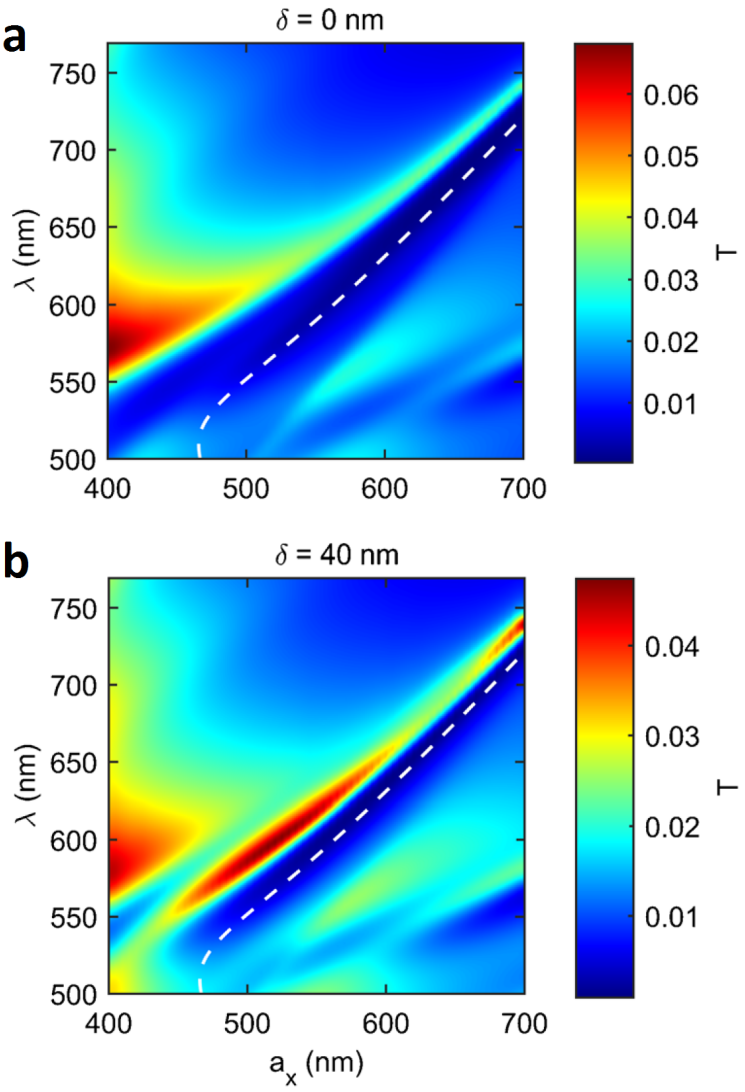

Fig. 5.9: Colormaps of the amount of light transmitted through bare nanohole arrays as a function of periodicity a_x and λ for **a** δ=0 nm **b** δ=40 nm. The white dashed line represents the theoreticaly calculated values of the resonance wavelength λ_{res}.

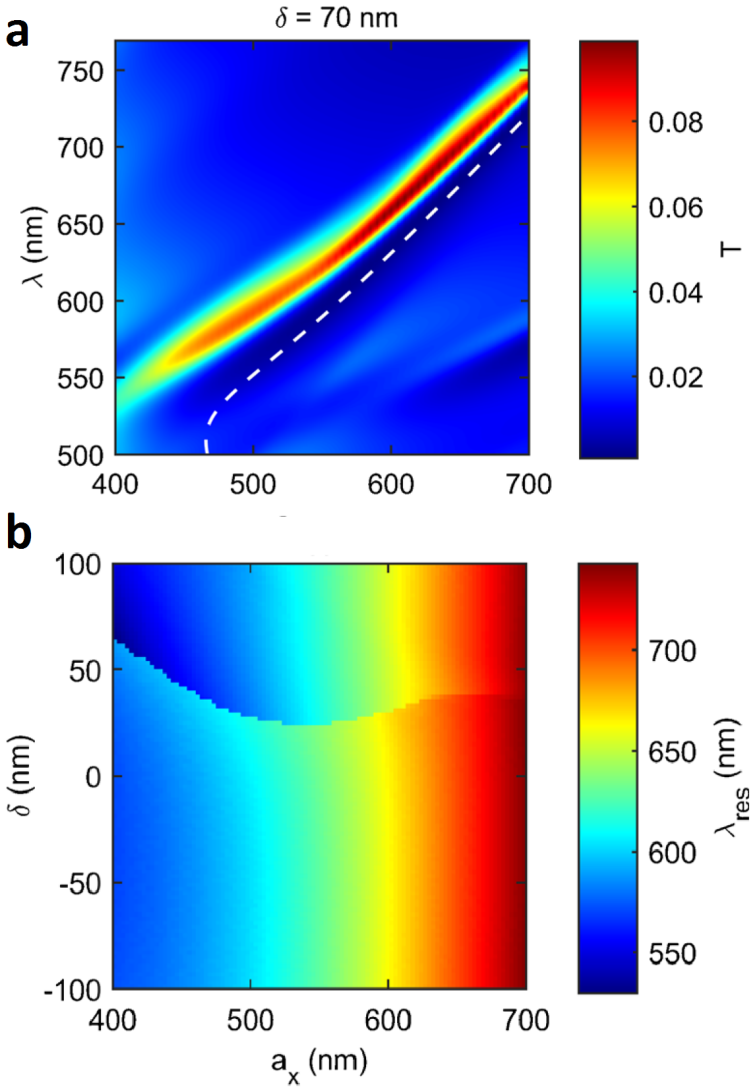

Fig. 5.10: **a** Colormap of the amount of light transmitted through bare nanohole arrays as a function of periodicity a_x and λ for δ=70 nm. The white dashed line represents the theoreticaly calculated values of the resonance wavelength λ_{res}. **b** Resonance wavelength λ_{res} as a function of periodicity a_x and parameter δ.

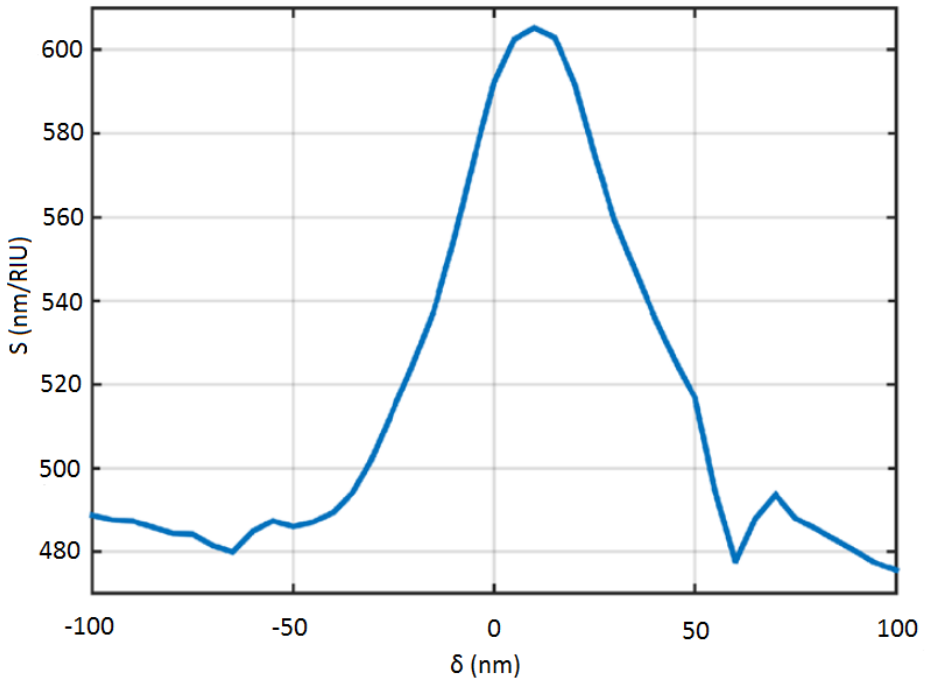

Fig. 5.11: Sensitivity S of the nanohole array with rectangular lattice configuration as a function of δ, for a_x=500 nm and n_d=1.33.

Figure 5.9b also clearly shows that, with increasing a_x, the resonance wavelength is suddenly shifted to lower wavelengths. This is the direct consequence of the resonance splitting that was mentioned earlier in this section.

In Figure 5.10b, the resonant wavelengths are displayed as a function of a_x and δ. In the regions where peak splitting occurs, the peak with larger transmission is chosen. We can see that, with increasing a_x, the shift of the λ_{res}, located at the discontinuities in the colormap, is decreasing and eventually disappears. Therefore we can assume, that for sufficiently large values of a_x, no splitting phenomenon could be observed at all.

5.3 Bulk sensor

In this section, the influence of δ on the sensing capability of the apertures defined by its sensitivity S, FWHM and FOM of the nenohole array immersed in some bulk medium (defined with its refractive index n_d) is investigated.

Figures 5.11, 5.12 and 5.13 shows the dependence of S, FOM and FWHM as a function of δ, respectively. Here, a_x=500 nm and the system is immersed in water with refractive index n_d=1.33.

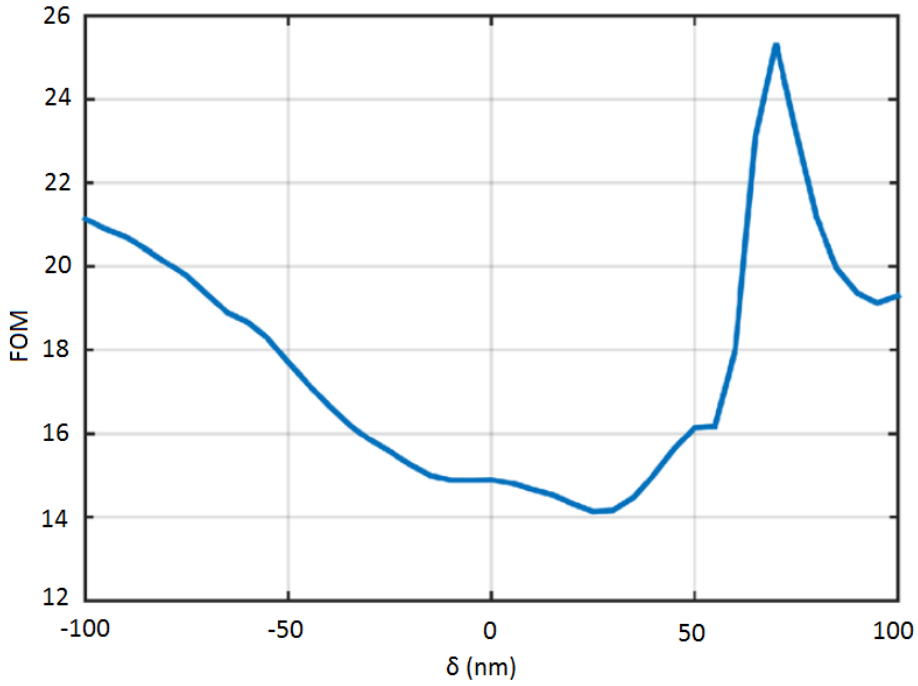

Fig. 5.12: FOM of the nanohole array with rectangular lattice configuration as a function of δ, for a_x=500 nm and n_d=1.33.

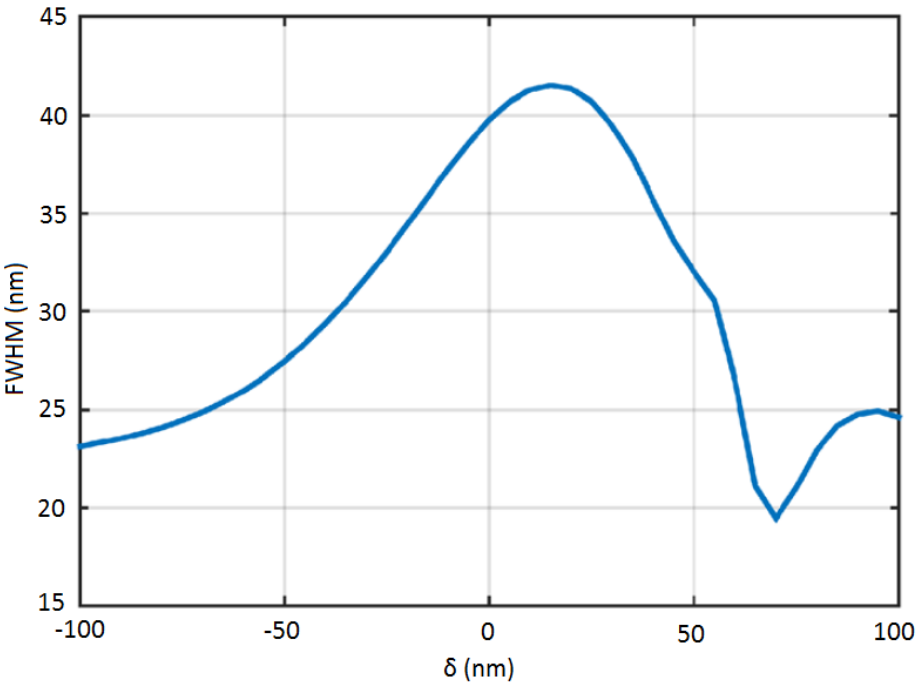

Fig. 5.13: FWHM of the nanohole array with rectangular lattice configuration as a function of δ, for a_x=500 nm and n_d=1.33.

By deviation from the square lattice, the system shows decrease in sensitivity, but with decreasing δ to the negative values, we can observe fast decrease in the FWHM and for example by choosing large negative value of δ could significantly improve FOM incomparison to standard square lattice configuration, and therefore the sensing capabilities. Moreover, such lattice geometry shows also larger transmission, which is advantegous for systems that are using imaging-based devices.

5.4 Surface sensor

Figures 5.14, 5.15 and 5.16 shows the examples of the transmission spectra of the nanohole array in air (vacuum, n=1) and array covered with a thin dielectric layer, mimicking protein-like structure immobilized on the surface, for δ=-100 nm, δ=0 nm and δ=35 nm, respectively. The dielectric layer has a thickness of 10 nm and refractive index n_d=1.6.

We can see, that for square lattice (δ=0 nm, Fig. 5.15), the spectral shift of the resonance caused by the dielectric layer is $\Delta\lambda_{res}$=18 nm. The FWHM of the transmission resonance is then 58 nm, giving us $\Delta\lambda_{res}$/FWHM ratio of 0.31. Using a nanohole array with large negative value of δ, as shown in Fig. 5.14, we can observe slightly bigger resonance shift of $\Delta\lambda_{res}$=21 nm, but significantly greater transmission and smaller value of FWHM. These "well-defined" peaks then gives us much greater $\Delta\lambda_{res}$/FWHM ratio of 0.45.

However, by utilizing a rectangular lattice with certain δ values, the sensitivity can be enhanced even further. In case of δ=35 nm, as shows Fig. 5.16, the results show much greater resonance shift of λ_{res}=45 nm. The mode with the highest transmission is allways considered. In the case of the bare nanohole system, the resonance with the highest transmission is observed at shorter wavelengths ($\lambda_{2,res}$),while after the addition of the dielectric film, the resonance with the highest transmission is observed now at longer wavelengths ($\lambda_{1,res}$). This means that, for certain range of δ, the spectral distance of the compared transmission peaks is greatly enhanced. Although the FWHM of the transmission resonance is bigger (58 nm) in this case, we still observe much larger $\Delta\lambda_{res}$/FWHM ratio of 0.77, and therefore significantly better sensing capabilities.

The range of δ, where we can achieve this enchanced characteristics, can be seen on Figures 5.17a and 5.17b, where the $\Delta\lambda_{res}$/FWHM is shown as a function of δ and a_x. This region is located between the two discontinuities on each figure. The discontinuity located at lower values of δ corresponds to the resonance splitting of the bare nanohole array while the discontinuity at higher values of δ corresponds to the splitting of the system after addition of the 10 nm thin dielectric layer.

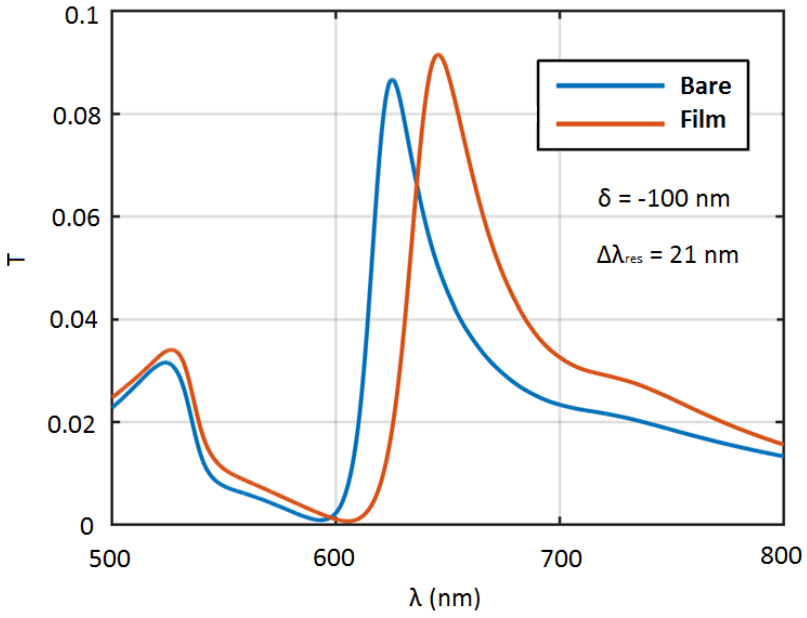

Fig. 5.14: Transmission spectra of the nanohole array before (blue line) and after (red line) the addition of a 10 nm thick dielectric layer for period a_x=540 nm and δ=-100 nm.

Figure 5.17a also shows that, for (a_x, δ) pairs which are not located between the two discontinuities, $\Delta\lambda_{res}$ behaves as in the case of the square lattice. However, as we observed in previous sections, decreasing δ to large negative values can improve the quality of the resonance. Figure 5.17b shows that this effect is the strongest for $a_x \approx 550$ nm, where we observe an improvement in $\Delta\lambda_{res}$/FWHM ratio caused by narrowing the resonance linewidth.

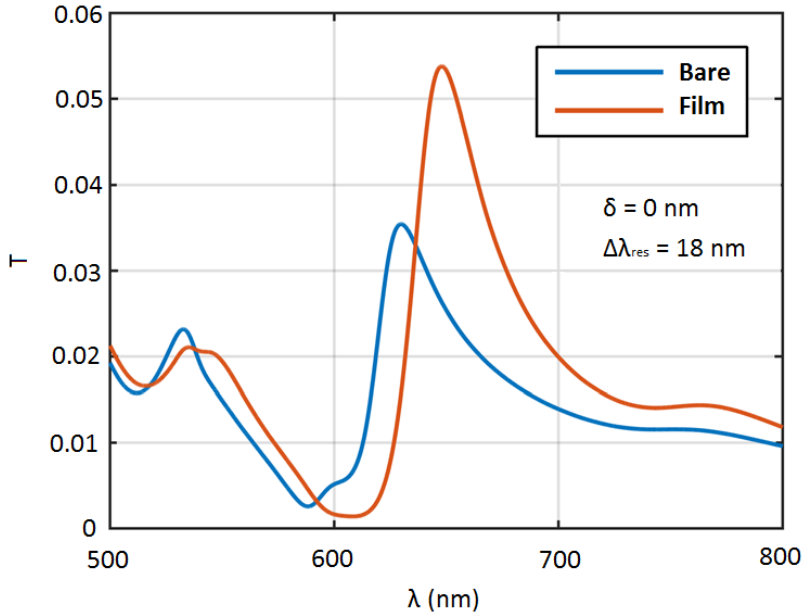

Fig. 5.15: Transmission spectra of the nanohole array before (blue line) and after (red line) the addition of a 10 nm thick dielectric layer for period a_x=540 nm and δ=0 nm.

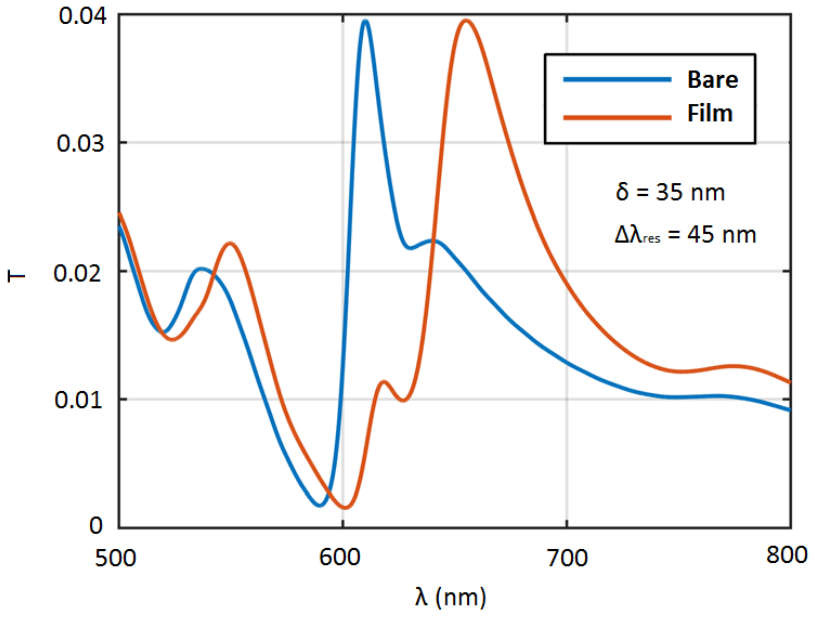

Fig. 5.16: Transmission spectra of the nanohole array before (blue line) and after (red line) the addition of a 10 nm thick dielectric layer for period a_x=540 nm and δ=35 nm.

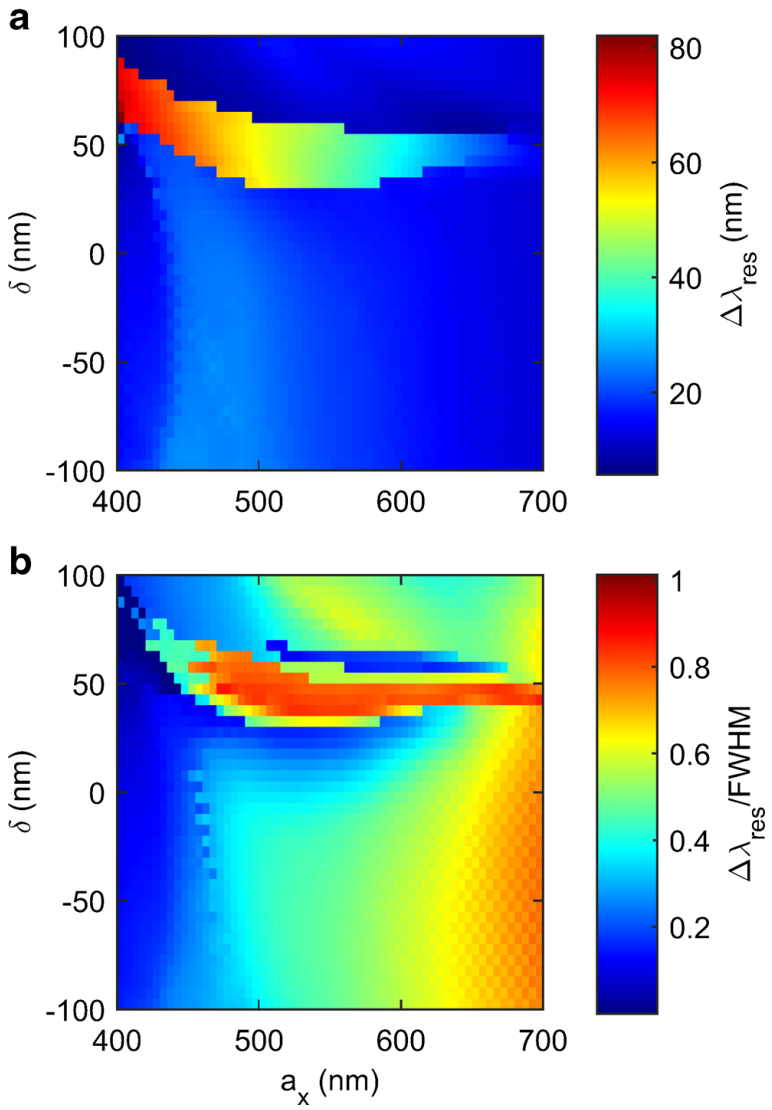

Fig. 5.17: **a** Shift in the resonance wavelength $\Delta\lambda_{res}$ caused by the addition of thin dielectric layer on the golden surface and **b** $\Delta\lambda_{res}$/FWHM ratio of the nanohole array as a functions of a_x and δ.

6 CONCLUSION

The goals of this diploma thesis were to select a suitable type of the EOT sensor, by definition of the material system and choice of the nanohole array, and to investigate the influence of the geometric parameters on its sensitivity and other possible detection characteristics.

In the first four chapters, the theoretical knowledge that forms the basis for plasmonic sensing applications was introduced as well as the basic introduction to the FDTD numerical method, that was used to carry out the simulations in this thesis.

In the second part of this work, we study the EOT properties of nanohole arrays with a rectangular lattice for label-free refractive index sensing applications. The description is based on our results that were published in [31]. All the selected parameters, that define the material system and nanohole array, are chosen with respect to real experiments [13, 42, 67] and can not be significantly changed for technological reasons.

First, the influence of the nanohole diameter and the thickness of the Au, SiN and Ti layers on the resonance transmission and the shape of the EOT peak was investigated. Here, the results showed that all of the parameters should be chosen very carefully. However, thinner SiN layer as well as larger values of the Au layer thickness and hole diameter showed the most promising results.

The influence of the periodicities of the nanohole array in two axes was then investigated. We showed that, by deviating from the standardly used square configuration of the nanohole array, we can increase the resonance transmission and decrease the resonance linewidth (FWHM), which can significantly improve the sensing cpabilities of such system, especially for large negative values of δ parameter defined as the difference between periodicities in both axes. The splitting of the resonance peak was also observed for certain values of δ, caused by transmission dominance of the second transmission resonance located at lower wavelengths.

Next, the sensitivity, FWHM and the field of merit (FOM) of the nanohole array immersed in some bulk medium as a function of δ is investigated. Although the sensitivity is greatest for values of δ very close to zero, the choice of large negative value of δ is preferable, because of the narrowing of the EOT linewidth, and therefore significant increase in the FOM.

In the last part of the simulations, we investigated the influence of δ on the sensing capabilities of nanohole arrays with the presence of the thin dielectric layer that mimicks biomolecules immobilized on the golden surface. The large negative values of δ, again, showed very promising results. However, results showed, that the resonance splitting of the bare nanohole array occurs at lower values of δ then

in the case where the dielectric layer is present. This leads to the presence of a region between certain δ values, where the spectral shift of the resonance is greatly enhanced. Although the FWHM values are greater in this case, the system still shows increase in $\Delta\lambda_{res}$/FWHM ratio, leading to significantly better sensing capabilities of such systems.

We believe, that the results presented in this work could provide an effective way to select the most advantageous lattice configuration to realize biodetection platforms providing the highest sensitivities.

Symbols

$\vec{E}$...Electric field
$\vec{B}$...Magnetic induction
$\vec{D}$...Dielectric displacement
$\vec{H}$...Magnetic field
T...Light transmission
λ...Wavelength
$\vec{j}$...Current density
$\vec{k}$...Wavevector
ρ...Electric charge density
μ...Relative permeability
ϵ...Relative permittivity
$\vec{P}$...Polarization
$\vec{M}$...Magnetization
n...Refractive index
κ...Extinction coefficient
τ... Relaxation time
γ...Collision frequency
ω...Frequency
u...Displacement of the electron gas
β....Propagation constant

Shorts

FDTD - Finite Difference Time Domain
EOT - Extraordinary Optical Transmission
SPP - Surface Plasmon Polariton
LPP - Localized Surface Plasmon
TM - Transverse Magnetic
TE - Transverse Electric
SNOM - Scanning Near-field Optical Microscopy
SEF - Surface Enhanced Fluorescence
SERS - Surface Enhanced Raman Spectroscopy
UPML - Uni-axial Perfectly Matched Layers
PBC - Periodic Boundary Conditions
FWHM - Full Width at Half Maximum
FOM - Field Of Merit

LITERATURE

[1] Antoine Lesuffleur, Hyungsoon Im, Nathan C. Lindquist, Kwan Seop Lim, and Sang-Hyun Oh. Laser-illuminated nanohole arrays for multiplex plasmonic microarray sensing. *Optics express*, 16(1):219–224, 2008.

[2] Bethe H. A. Theory of diffraction by small holes, 1944.

[3] T. W. Ebbesen, H. F. Ghaemi, and T. Thio. Extraordinary optical transmission through sub-wavelength hole arrays. 391(February):667–669, 1998.

[4] Reuven Gordon, Alexandre G. Brolo, David Sinton, and Karen L. Kavanagh. Resonant optical transmission through hole-arrays in metal films: Physics and applications. *Laser and Photonics Reviews*, 4(2):311–335, 2010.

[5] V. G. Rivera, F. Ferri, O. B. Silva, F. W. Sobreira, and E. Marega Jr. Light Transmission via Subwavelength Apertures in Metallic Thin Films. *Plasmonic-Principles and Applications*, page 26, 2012.

[6] P. Marthandam and R. Gordon. Polarization-controlled diffraction from a quasicrystal nanohole array in a gold film. *Journal of Optics A: Pure and Applied Optics*, 9(12):1140, 2007.

[7] R. Gordon, A. G. Brolo, A. McKinnon, A. Rajora, B. Leathem, and K. L. Kavanagh. Strong Polarization in the Optical Transmission through Elliptical Nanohole Arrays. *Phys. Rev. Lett.*, 92(3):37401, 2004.

[8] Chih-ming Wang, Yia-chung Chang, and Mohammed Nadhim Abbas. T-shaped plasmonic array as a narrow-band thermal emitter or biosensor. 17(16):363–365, 2009.

[9] R. C. McPhedran and D. Maystre. On the theory and solar application of inductive grids. *Applied physics*, 14(1):1–20, 1977.

[10] Yongdong Liu and Steve Blair. Fluorescence enhancement from an array of subwavelength metal apertures. *Opt. Lett.*, 28(7):507–509, 2003.

[11] Martin Moskovits. Surface-enhanced spectroscopy. *Rev. Mod. Phys.*, 57(3):783–826, 1985.

[12] E. Altewischer, M. P. van Exter, and J. P. Woerdman. Plasmon-assisted transmission of entangled photons. *Nature*, 418(6895):304–306, jul 2002.

[13] Arif E. Cetin, Ahmet F. Coskun, Betty C. Galarreta, Min Huang, David Herman, Aydogan Ozcan, and Hatice Altug. Handheld high-throughput plasmonic biosensor using computational on-chip imaging. (April 2013), 2014.

[14] Oliver Benson. Plasmonics. *Elements of Nanophotonics*, pages 208–239, 2009.

[15] Stefan A. Maier. *Plasmonics : Fundamentals and Applications*, volume 677. 2004.

[16] David B. Tanner. Optical effects in solids. pages 1–245, 2013.

[17] Max Born and Emil Wolf. *Principles of optics - electromagnetic theory of propagation, interference and diffraction of light*. University of Cambridge, 7th edition, 2003.

[18] David J. Griffiths. Introduction to electrodynamics. *Tensor*, 1999.

[19] B.V. Paranjape and M.B. Paranjape. On the interaction of electromagnetic waves with conductors. *Canadian Journal of Physics*, 90(9):849–853, 2012.

[20] Charles Kittel and Paul McEuen. *Introduction to solid state physics*, volume 8. 1986.

[21] P.W. Johnson and R.W. Christy. Optical constants of the noble metals. *Phys. Rev. Lett.*, 6(12):4370–4379, 1972.

[22] Anatoly V. Zayats, Igor I. Smolyaninov, and Alexei A. Maradudin. Nano-optics of surface plasmon polaritons. *Physics Reports*, 408(3-4):131–314, 2005.

[23] W. L. Barnes, A. Dereux, and T. W. Ebbesen. Surface plasmon subwavelength optics. *Nature*, 424(6950):824–30, 2003.

[24] Erwin Kretschmann. Die Bestimmung optischer Konstanten von Metallen durch Anregung von Oberflächenplasmaschwingungen, url = http://dx.doi.org/10.1007/BF01395428, volume = 241, year = 1971. *Zeitschrift für Physik A Hadrons and nuclei*, (4):313–324.

[25] A. Otto. Excitation of nonradiative surface plasma waves in silver by the method of frustrated total reflection. *Z. Physik*, 216:398, 1968.

[26] A. Edelmann and S. F. Helfert. Excitation of surface plasmon polaritons using prism coupling. 410:1988, 1988.

[27] Jan Renger, Romain Quidant, Niek Van Hulst, Stefano Palomba, and Lukas Novotny. Free-Space excitation of propagating surface plasmon polaritons by nonlinear Four-Wave mixing. *Physical Review Letters*, 103(26):1–4, 2009.

[28] F. López-Tejeira, Sergio G. Rodrigo, L. Martín-Moreno, F. J. García-Vidal, E. Devaux, T. W. Ebbesen, J. R. Krenn, I. P. Radko, S. I. Bozhevolnyi, M. U. González, J. C. Weeber, and A. Dereux. Efficient unidirectional nanoslit couplers for surface plasmons. *Nature Physics*, 3(5):324–328, 2007.

[29] Alexandre Bouhelier and Lukas Novotny. Chapter 10 - Near-field optical excitation and detection of surface plasmons.

[30] Stephanie Law, Viktor Podolskiy, and Daniel Wasserman. Towards nano-scale photonics with micro-scale photons : the opportunities and challenges of mid-infrared plasmonics. 2(2):103–130, 2013.

[31] Arif E. Cetin, Yasa Eksioglu, Jiří Petráček, and Martin Dršata. Extraordinary Transmission Characteristics of Subwavelength Nanoholes with Rectangular Lattice. (26), 2016.

[32] Paras N. Prasad. *Introduction to biophotonics.*

[33] P. N. Patel, V. Mishra, and A. S. Mandloi. Optical Biosensors : Fundamentals & Trends. *Journal of Engineering Research and Studies*, I(I):15–34, 2010.

[34] Jing Zhao, Aditi Das, George C. Schatz, Stephen G. Sligar, and Richard P. Van Duyne. Resonance localized surface plasmon spectroscopy: Sensing substrate and inhibitor binding to cytochrome P450. *Journal of Physical Chemistry C*, 112(34):13084–13088, 2008.

[35] Yanan Wang, Archana Kar, Andrew Paterson, Katerina Kourentzi, Han Le, Paul Ruchhoeft, Richard Willson, and Jiming Bao. Transmissive nanohole arrays for massively-parallel optical biosensing. *ACS Photonics*, 1(3):241–245, 2014.

[36] Y. Eksioglu and Cetin A.E. Optical response of plasmonic nanohole arrays comparsion of square and hexagonal lattices.

[37] A-P. Blanchard-Dionne, L. Guyot, S. Patskovsky, R. Gordon, and M. Meunier. Intensity based surface plasmon resonance sensor using a nanohole rectangular array. *Optics express*, 19(16):15041–6, 2011.

[38] Dye Zone A. Chen, Rafif Hamam, Marin Soljačić, John D. Joannopoulos, and Gang Chen. Extraordinary optical transmission through subwavelength holes in a polaritonic silicon dioxide film. *Applied Physics Letters*, 90(18):5–7, 2007.

[39] Antoine Lesuffleur, Hyungsoon Im, Nathan C. Lindquist, Kwan Seop Lim, and Sang-Hyun Oh. Plasmonic Nanohole Arrays for Real-Time Multiplex Biosensing. *Proc. SPIE*, 7035:703504–703510, 2008.

[40] L. Martin-Moreno and F. J. Garcia-Vidal. Optical transmission through circular hole arrays in optically thick metal films. *Optics Express*, 12(16):3619, 2004.

[41] Feng Long, Anna Zhu, and Hanchang Shi. Recent advances in optical biosensors for environmental monitoring and early warning. *Sensors (Basel, Switzerland)*, 13(10):13928–13948, 2013.

[42] Ahmet Ali Yanik, Arif E. Cetin, Min Huang, Alp Artar, S. Hossein Mousavi, Alexander Khanikaev, John Connor, Gennady Shvets, and Hatice Altug. Ultrasensitive plasmonic fano sensor enables seeing protein monolayers with naked eye. *IEEE Photonic Society 24th Annual Meeting, PHO 2011*, 108(29):425–426, 2011.

[43] Xudong Fan, Ian M. White, Siyka I. Shopova, Hongying Zhu, Jonathan D. Suter, and Yuze Sun. Sensitive optical biosensors for unlabeled targets: A review. *Analytica Chimica Acta*, 620(1-2):8–26, 2008.

[44] Dennis M. Sullivan and David T. Borup. Use of the Finite-Difference Time-Domain Method Calculating EM Absorption in Human Tissues. (2):148–157, 1987.

[45] D.M. Sheen and M.A. Sami. Application of the Three-Dimensional Method to the Analysis of Planar Microstrip Circuits. (7), 1990.

[46] Ping Yang and K. N. Liou. Finite-difference time domain method for light scattering by small ice crystals in three-dimensional space. 13(10):2072–2085, 1996.

[47] K. Yee. Numerical solution of initial boundary value problems involving Maxwell's equations in isotropic media, 1966.

[48] A. Taflove and M.E. Brodwin. Numerical solution of steady-state electromagnetic scattering problems using the time-dependent Maxwell's equations. *IEEE Transactions on Microwave Theory and Techniques*, 8(23):623–630, 1990.

[49] F. Michael Kahnert. *Numerical methods in electromagnetic scattering theory*, volume 79-80. 2003.

[50] Allen Taflove. *Computational Electrodynamics: The Finite-Difference Time-Domain Method*. Artech House, 1995.

[51] Umran S. Inan and Robert A. Marshall. *Numerical Electromagnetics: The FDTD Method*. 2011.

[52] Mario Fusco. FDTD Algorithm in Curvilinear Coordinates. 38(I):76–89, 1990.

[53] Richard Holland, Vaughn P. Cable, and Louis C. Wilson. Techniques for EM Scattering. 33(4), 1991.

[54] J. Lee. Numerical solutions of TM scattering using an obliquely Cartesian finite difference time domain algorithm.

[55] Natalia K. Nikolova. The Finite-Difference Time-Domain (FDTD) method - part I. pages 1–25, 2011.

[56] David E. Merewether. Transient Currents Induced on a Metallic Body of Revolution by an Electromagnetic Pulse. (2):41–44, 1971.

[57] S.T. Chu and S.K. Chaudhuri. Finite-Difference Time-Domain method for optical waveguide analysis, 1995.

[58] Richard Holland. Finite-difference solution of Maxwell's equations in gerneralized nonorthogonal coordinates. (6):4589–4591, 1983.

[59] Jean-Pierre Berenger. A perfectly matched layer for the absorption of electromagnetic waves, 1994.

[60] Weng Cho Chew and William H Weedon. A 3-D Perfectly Matched Medium from Modified Maxwell's Equations with Stretched Coordinates. 7(13):599–604.

[61] John Schneider. Understanding the Finite-Difference Time-Domain Method. *Artech House antennas and propagation library*, 2010(2):1006, 2005.

[62] Z.-Y. Huang, L.-H. Shi, Y. Zhou, and B. Chen. UPML-ABC and TF/SF boundary for unconditionally stable AH-FDTD method in conductive medium. *Electronics Letters*, 51(21):1654–1656, 2015.

[63] Valery V. Tuchin. FDTD Simulation of Light Interaction with Cells for Nanobiophotonics Diagnostics and Imaging. 2010.

[64] www.lumerical.com.

[65] Fan Yang, Ji Chen, Rui Qiang, and Atef Elsherbeni. A simple and efficient FDTD / PBC algorithm for scattering analysis of periodic structures. 42(July):1–9, 2007.

[66] Dongying Li and Costas D. Sarris. FDTD lattice termination with periodic boundary conditions. *IEEE MTT-S International Microwave Symposium Digest*, (1):329–332, 2009.

[67] Ahmet A. Yanik, Min Huang, Osami Kamohara, Alp Artar, Thomas W. Geisbert, John H. Connor, and Hatice Altug. An optofluidic nanoplasmonic biosensor for direct detection of live viruses from biological media. *Nano Letters*, 10(12):4962–4969, 2010.

[68] David R. Lide Ed. CRC Handbook of Chemistry and Physics, 84th Edition, 2003-2004.